Physics Program

Master Thesis

Preparatory studies on the determination of the top-quark mass in single top-quark events with the ATLAS detector at the LHC

Prepared by:
Shayma' Wahdan

Supervised by:
Dr. Wafaa Khater[1], Prof. Dr. Wolfgang Wagner[2]

1. Birzeit university - Palestine, 2. Bergische Universität Wuppertal - Germany

Birzeit, Palestine

June 2017

Preparatory studies on the determination of the top-quark mass in single top-quark events with the ATLAS detector at the LHC

دراسات تحضيرية لقياس كتلة كوارك القمة الذي تم إنتاجه باستخدام مكشاف أطلس في مسارع الهادرونات الكبير

By
Shayma' Abderra'ouf Hosain Wahdan

This Thesis was submitted in partial fulfillment of the requirements for the Master's Degree in physics From the Faculty of Graduate Studies at Birzeit University, Palestine

Thesis committee:

Dr. Wafaa Khater (Local Principal Advisor)

Prof. Dr. Wolfgang Wagner (External Advisor)

Dr. Wael Karain (Member)

Dr. Hazem Abusara (Member)

June 2017

Preparatory studies on the determination of the top-quark mass in single top-quark events with the ATLAS detector at the LHC

دراسات تحضيرية لقياس كتلة كوارك القمة الذي تم إنتاجه باستخدام مكشاف أطلس في مسارع الهادرونات الكبير

By

Shayma' Wahdan

Accepted by the Faculty of Graduate Studies, Birzeit University, in partial fulfillment of the degree of Master of physics

Thesis committee:

Wafaa Khater Ph.D. (Local Principal Advisor)

Wolfgang Wagner Ph.D. (External Advisor)

Wael Karain Ph.D. (Member)

Hazem Abusara Ph.D. (Member)

Abstract

In this thesis, a measurement of the single top quark mass produced in the t -channel is presented, using the data sample recorded recently in 2015 with the ATLAS detector at the LHC, at a centre of mass energy of $\sqrt{s} = 13$ TeV and corresponding to an integrated luminosity of 3.2 fb^{-1}. The selected events contain one charged lepton (electron or muon), missing transverse energy, and two jets with high transverse momentum with one of them being b-tagged.

The template method is used to extract the top quark mass from the distribution of the invariant mass of the lepton and the b-jet ($m(\ell b)$) in the selected events. The result of the measured top quark mass is: $m_{top} = [174.56 \pm 3.11(syst.) \pm 1.02(stat.)]$ GeV.

ملخص

في هذه الرسالة تم عرض قياس كتلة كوارك القمة الذي تم إنتاجه عن طريق القوة الضعيفة والذي يتفكك فيه إلى كل من كوارك القاع و W بوزون، حيث يتفكك الأخير إلى ليبتون (إلكترون أو ميون) والنيوترينو المصاحب ل الليبتون. باستخدام مكشاف أطلس في مسارع الهادرونات الكبير(LHC) . عند طاقة مركز الكتلة ١٣ تيرا إلكترون فولت. تم اختيار التفاعلات التي تحتوي على ليبتون مشحون واحد، وطاقة ضائعة، واثنين jets أحدهما مقترن بكوراك القاع ولها كمية تحرر عمودية كبيرة.

استخدمت طريقة ال Template للحصول على الكتلة المطلوبة من خلال معرفة توزيع كتلة اللبتون وال b-jet حيث كانت النتيجة ١٧٤،٥٦ جيجا إلكترون فولت بمقدار خطأ حسابي ٣،١١ جيجا إلكترون فولت و إحصائي ١،٠٢ جيجا إلكترون فولت.

Acknowledgement

First of all, I thank Allah for giving me the power to believe in my passion and pursue my dreams.

A very special thanks to Professor Wolfgang Wagner for being my first supervisor and giving me the opportunity to do this analysis at **Bergische Universität Wuppertal** in Germany, as well as for his help, care and support.

A big thank to Dr. Dominic Hirschbül for the time he gave to me and answering all my questions in physics and in programming. Also I want to thank all the particle physics group in Wuppertal university, especially Arwa Bannoura, Gunnar Jäkel, Marcelo Vogel, Nicolas Lang, and Phillip Teppel, for many useful and productive discussions I had with them.

And of course a great thanks to Dr. Wafaa Khater for being my supervisor from Birzeit university, for her courage and support. To Dr. Hazem Abusara, and Dr. Wael Karain for being part of the thesis defence, reading and assessing. Beside to being my teachers and giving me a lot of information over the last six years. As well as many other teachers at Birzeit university in my Bachelor and Master studies.

Heartiest thanks for my friends, especially my close friends.

Last but not least I want to send my warm and sincere to my parents, my sisters and brothers, for always providing me a place I can escape to when everything goes wrong, for their support throughout all over the years in my life.

Declaration

I certify that this thesis, submitted for the degree of Master of Physics to the department of Physics at Birzeit University, is my own research except where otherwise acknowledged, and that this thesis (or any part of it) has not been submitted for a higher degree to any other university or institution.

Shayma' Wahdan
Signature.....

Contents

1 Introduction **1**

2 Top-quark physics **2**
2.1 The standard model . . . 2
2.1.1 Matter particles . . . 2
2.1.2 Forces and gauge bosons . . . 3
2.1.3 The Higgs boson . . . 4
2.2 Top quark production . . . 5
2.2.1 Top-antitop quark pair production . . . 5
2.2.2 Single top quark production . . . 5
2.2.3 Single top quark decays . . . 6
2.3 The mass of the top quark . . . 6
2.3.1 Motivation for the top quark mass measurements . . . 8
2.3.2 The template method to measure the top quark mass . 10

3 LHC and the ATLAS Detector **12**
3.1 The ATLAS detector . . . 14
3.1.1 The inner (tracking) detector . . . 15
3.1.2 Calorimeters . . . 17
3.1.3 The muon spectrometer . . . 17

4 Monte Carlo Simulations **19**
4.1 Event generation . . . 20
4.1.1 Monte Carlo generators . . . 21
4.1.2 Monte Carlo Samples . . . 22
4.2 Detector simulation . . . 25

5 Physics Objects Reconstruction **26**
5.1 Charged leptons reconstruction . . . 27
5.2 Jets reconstruction . . . 27
5.2.1 *b*-jet reconstruction . . . 28

5.3 Missing transverse momentum reconstruction 29
5.4 Top quark reconstruction 29

6 Processes Description **31**
6.1 The Dataset 31
6.2 Event selection 32
6.3 Signal processes 32
6.4 Background processes 33
6.5 Signal and background discrimination 34
6.5.1 Neural Network 35
6.5.2 Input variables 36
6.5.3 Cutting on the neural network output 37
6.5.4 Event yields 38

7 Mass Measurements **39**
7.1 The template method 39
7.1.1 $m(\ell b)$ observable 40
7.1.2 Construction of the fitting templates 40
7.1.3 Top quark mass dependence on $m(\ell b)$ 42
7.1.4 Likelihood fit to extract m_{top} 43
7.2 Method validation 45
7.3 Systematic uncertainties 47
7.3.1 Object energy scale/resolution and efficiencies uncertainties 47
7.3.2 Pileup re-weighting uncertainty 49
7.3.3 Simulation modelling uncertainties 50
7.3.4 Backgrounds rate 50
7.3.5 Summary 51
7.4 Statistical uncertainty 52

8 Results and Conclusion **53**

List of Figures

2.1 Elementary particles of the Standard Model [2]. 3
2.2 Potential of the Higgs field [5]. 4
2.3 Feynman diagrams for the modes of $t\bar{t}$ production: (a) and (b) via gluon-gluon fusion, (c) via quark anti-quark annihilation [8]. 5
2.4 Feynman diagrams for the single top quark production modes: (a) t-channel, (b) s-channel, (c) Wt-channel [8]. 6
2.5 Feynman diagram for single top quark production in the t-channel. The decay products of the single top are shown where the W-boson decays leptonically. 6
2.6 The top quark mass value obtained from the combined result of the ATLAS and CMS (LHC) [11]. 7
2.7 SM vacuum phase diagram showing different regions: absolute stability, meta-stability and instability of the SM vacuum, and non-perturbativity of the Higgs quartic coupling. (b) Zoom in the region of the preferred experimental range of m_{top} and m_H where the allowed uncertainties at 1, 2 and 3σ are represented by the gray area [13]. 8
2.8 Feynman diagram shows the cancellation of the Higgs boson quadratic mass between top quark loop and stop squark tadpole in SUSY [14]. 9
2.9 Scan of fits with fixed variables m_W vs. m_{top}. The result of the fit are: in blue including the m_H allowed region, in gray excluding m_H allowed region. The green bands and ellipse for the m_W and m_{top} direct measurements within 1σ [15]. 10
2.10 Sketch of templates of a variable $O(m_{top})$ which show a mass dependence. This variable has different distributions for different input m_{top}. 11
2.11 The template method steps to extract m_{top}. 11

3.1 Overall view of the LHC four experiments [21]. 13

3.2 Overview of the ATLAS detector [22]. 14
3.3 ATLAS detector coordinate system [23]. 15
3.4 ATLAS Inner Detector [24]. 16
3.5 ATLAS Calorimeter system [25]. 17
3.6 ATLAS Muon Spectrometer [26]. 18

4.1 Monte Carlo simulated events generation process. 19
4.2 The basic structure of a hard hadron scattering MC event [28]. 21

5.1 The trajectories of different particles in the ATLAS experiment [44]. 26
5.2 Schematic view of the b-hadron decay [50]. 28

6.1 Total Integrated Luminosity between June and November 2015 [53]. 31
6.2 Feynman diagrams of (a) W+jets, (b) Z+jets background processes [54]. 33
6.3 Feynman diagrams of the diboson background processes (a) WW, (b) WZ, (c) ZZ [54]. 34
6.4 Example of a QCD-multijet background feynman diagram [54]. 34
6.5 Schematic view of a three-layers feed-forward Neural Network [56]. 35
6.6 The NN output distribution: (a) shape distribution normalized to unit area, (b) simulated and observed distribution. . . 36
6.7 Fraction of the different processes: (a) before the NN cut, (b) after the NN cut $O_{NN} > 0.8$ 37

7.1 $m(\ell b)$ distribution after the NN output cut for the simulated signal and background processes. The black dots show the observed data. 40
7.2 $m(\ell b)$ simulated signal distributions for different input masses : (a) 170 GeV (b) 172.5 GeV, (c) 175 GeV. Fitted to the function defined in Eq. (7.1). 42
7.3 Mass dependent parameters, fitted with Eq. (7.2): (a) Landau mode (p_3) (b) Gaussian mean (p_5). 43
7.4 $m(\ell b)$ distribution for signal and background processes compared to data: (a) MC distribution with input mass 172.5 GeV compared to data, (b) fitted templates to the data after performing the binned maximum likelihood fit using the best fit of m_{top}. 44

7.5 Mass distribution generated from the pseudo datasets for input m_{top}: (a) 170 GeV, (b) 172.5 GeV, (c) 175 GeV. 46
7.6 The x-axis shows m_{top} the used m_{top} in the simulation, the y-axis: (a) the output mass of pseudo experiments $\langle m_{top}^{out} \rangle$, (b) the difference $m_{top} - \langle m_{top}^{out} \rangle$. 46
7.7 Example on how the systematic uncertainties are calculated. By varying the uncertainty source by $+1\sigma$ (red curve) and -1σ (light blue), where the nominal distribution in dark blue. 47
7.8 Number of interactions per crossing bunch. Data recorded in 2015 between 3 June till 3 November at $\sqrt{s} = 13$ TeV [65]. . 49
7.9 Mass distribution generated from the pseudo-datasets for m_{top} 172.5 GeV. 52

8.1 Statistical uncertainty for integrated luminosity values: 3.2, 36, 72 and 100 fb^{-1}. 54

List of Tables

2.1 The four fundamental forces with their relative strength and range. 3

3.1 Comparison of the LHC parameters during the 2015 operation and the design values [20]. 13

4.1 signal MC samples used in this analysis [34, 35]. 22
4.2 Diboson MC samples used in this analysis [36]. 23
4.3 W+jets MC samples used in this analysis [37–39]. 24
4.4 Z+jets MC samples used in this analysis [40–42]. 24

6.1 Input variables used in the NN training ordered by their discriminating power [55]. 36
6.2 Event yields and the fraction after the cut on the NN output, for the expected and the data events. 38

7.1 Parameters after fitting the $m(\ell b)$ distributions for the three input mass points: 170, 172.5, 175 GeV 41
7.2 Systematic uncertainties due to objects energy scale or resolution and the efficiencies uncertainties 48
7.3 Systematic uncertainties due to simulation modelling. 50
7.4 Summary of the systematic uncertainties. 51

8.1 sources of the systematic uncertainties. 53

Chapter 1

Introduction

The Standard Model of Particle physics describes the laws which control our universe at the smallest scale, by describing the elementary particles that represent the building blocks of matter and their interactions.

The **L**arge **H**adron **C**ollider (**LHC**) is the most powerful particle accelerator machine in the world. It started to operate in 2008 and currently is operating at an energy of 13 TeV. It is designed to test particle theories and hopefully observe new particles, using four major experiments called: ATLAS, CMS, LHCb, and ALICE. This analysis is done using the 2015 dataset recorded by ATLAS, with a center of mass energy of 13 TeV and an integrated luminosity of 3.2 fb^{-1}.

The top quark plays a special role among the other quarks, since it is the heaviest known elementary particle. A precision measurement of its mass has important implications due to its significant contribution to the Higgs boson mass, the electroweak radiative correction, other particles predicted by beyond-standard-model (BSM) theories, as well as our universe and its stability.

This analysis presents the template method to measure the mass of single top quark produced in the t-channel. The thesis is organized in the following way: Chapter 2 describes the top-quark in the standard model, chapter 3 describes the ATLAS detector in the LHC, chapter 4 describes MC simulation techniques, chapter 5 is about the identification of some of the physics objects related to the top quark, chapter 6 describes the event selection, and signal and background processes, chapter 7 is about the mass measurement and the uncertainties calculations, and the results with conclusion are presented in chapter 8.

Chapter 2

Top-quark physics

2.1 The standard model

The Standard Model of particle physics (SM) is a theory of the elementary particles and their interactions. These particles are classified in two basic classes called fermions and bosons. The fermions, also called matter particles, have half-integer spin and include the quarks and the leptons. The bosons have an integer spin and include the force carriers and the Higgs boson. All of these particles are summarized in Fig. (2.1).

The elementary particles interact via four different forces: the gravitational, the electromagnetic, the weak and the strong force. All of these forces are part of the SM except for the gravitational force [1].

2.1.1 Matter particles

Quarks and leptons are the building blocks of the matter around us. Each of these two groups consists of six particles related in pairs or generations. The lightest and most stable particles make up the first generation, whereas the heavier and less stable particles belong to the second and third generations. All stable matter in the universe is made from particles that belong to the first generation; heavier particles quickly decay to the next most stable level. Quarks named as: up (u), down(d), charm(c), strange(s), top(t) and bottom(b). Leptons named as: electron(e), electron nutrino(ν_e), muon(μ), muon nutrino(ν_μ), tau(τ) and tau neutrino(ν_τ). The neutrinos are electri-

cally neutral and have very small mass. Fig. (2.1) summarize the elementary particles with the mass, charge and spin for each particle.

Each particle has its own anti-particle that has exactly the same properties as the corresponding particle, but opposite quantum numbers.

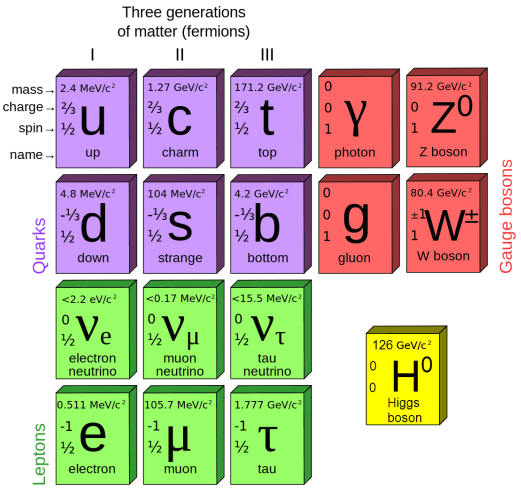

Figure 2.1: Elementary particles of the Standard Model [2].

2.1.2 Forces and gauge bosons

Four fundamental forces are exist in the nature: the strong, the weak, the electromagnetic, and the gravitational force. They work with different strengths over different ranges. The gravitational force is the weakest and can be neglected at the particle physics scale. The range and strength for each force are shown in Table 2.1.

Table 2.1: The four fundamental forces with their relative strength and range.

Force	**Relative strength**	**Range (m)**
Strong	10^{38}	10^{-15}
Electromagnetic	10^{36}	∞
Weak	10^{25}	10^{-18}
Gravitation	1	∞

Three of the fundamental forces result from the exchange of force-carrier particles shown in red in Fig. (2.1), which belong to a broader group called bosons. Each fundamental force has its own corresponding boson. The strong force is carried by the gluon; the electromagnetic force is carried by the photon, while the W and Z bosons are responsible for the weak force. The SM includes the electromagnetic, strong, and weak forces, and all their carrier particles, and explains well their interaction with the matter particles. However, the gravity force is not part of the SM.

These forces are described successfully as theories of quantum gauge symmetry, and they can be described in terms of unitary groups of different dimensions. The combination of gauge groups is $SU(3) \times SU(2) \times U(1)$. where $SU(3)$ is the symmetry group of the strong interaction, $SU(2)$ of the weak interaction and $U(1)$ of the electromagnetic.

2.1.3 The Higgs boson

The gauge bosons should be massive in order to keep the Standard Model re-normalisable. In 1964 Brout, Englert and Higgs proposed a spontaneously broken Higgs field spreading through the universe shown in Fig. (2.2). It shows how gauge bosons can acquire masses as a result of the spontaneous symmetry breaking within gauge invariant models of the universe.

The existence of such a field requires the existence of a particle that can excite such a field, so the scalar Higgs boson had been predicted until it was discovered in 2012 by the ATLAS and CMS experiments at the LHC [3, 4]. The Higgs boson is shown in Fig. (2.1) in yellow.

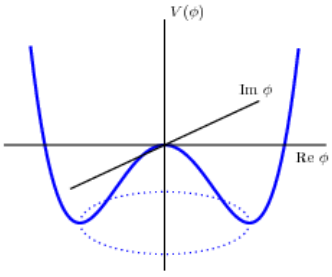

Figure 2.2: Potential of the Higgs field [5].

2.2 Top quark production

The top quark was discovered in 1995 at the TEVATRON collider in Fermilab by the CDF and Dϕ experiments [6, 7]. It is the most massive known elementary particle with a mass ≈ 173 GeV.

The top quark can be produced in two main processes: top-antitop quark pairs, or as a single top-quark.

2.2.1 Top-antitop quark pair production

The top anti-top quark pair ($t\bar{t}$) is produced via the strong interaction in two different channels: gluon-gluon fusion which is the most dominant at the LHC, and the quark anti-quark annihilation. Feynman diagrams are shown for both in Fig. (2.3), and they are following the convention that the x-axis corresponds to the time axis.

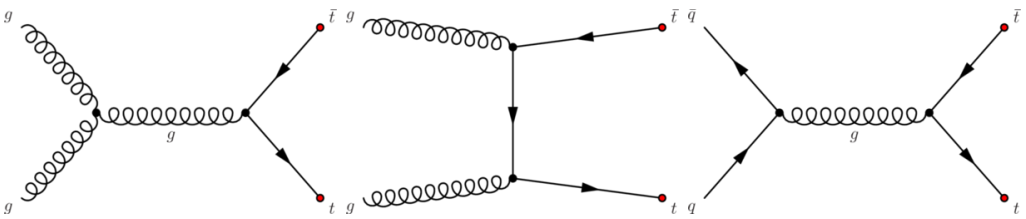

Figure 2.3: Feynman diagrams for the modes of $t\bar{t}$ production: (a) and (b) via gluon-gluon fusion, (c) via quark anti-quark annihilation [8].

2.2.2 Single top quark production

The single top quark is produced via the weak interaction in three different modes or channels. The t-channel which is the most dominant, the s-channel and the Wt-channel. Feynman diagrams are shown in Fig. (2.4).

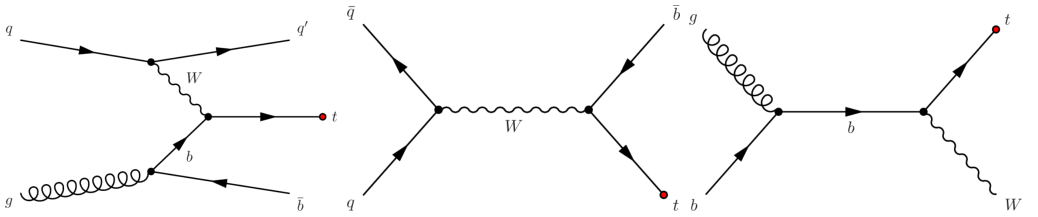

(a) (b) (c)

Figure 2.4: Feynman diagrams for the single top quark production modes: (a) t-channel, (b) s-channel, (c) Wt-channel [8].

2.2.3 Single top quark decays

As a result of the large mass of the top quark, it has a short lifetime $\approx 5 \times 10^{-25}$s and it cannot be detected directly. The single top quark decays with $\approx 100\%$ probability to b quark and W boson $\mathrm{t} \rightarrow \mathrm{W}^{\pm}\mathrm{b}$.

In this thesis, the t-channel topologies are studied where the $W^{\pm}$-boson decays leptonically. So the final state will be b-jet from the top quark decay, one charged lepton and missing transverse energy from the $W^{\pm}$-boson decay and an additional jet from the t-channel production itself, as illustratec in Fig. (2.5).

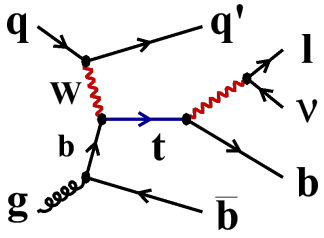

Figure 2.5: Feynman diagram for single top quark production in the t-channel. The decay products of the single top are shown where the W-boson decays leptonically.

2.3 The mass of the top quark

The definition of the mass of a quark is not straightforward, In Quantum Chromo Dynamic (QCD) this definition is known as the pole mass m_{top}^{pole} and

it is valid only in the perturbation regime. In this analysis m_{top} is defined as the measured value of the top quark mass as the input mass in the generation of the Monte Carlo samples. For this purpose, the invariant mass of the decay products of the single top t-channel decay can be reconstructed. Particles reconstructed within the detector are: one electron or muon, one light quark, detected as a jet of many particles pointing in one direction and one b-tagged jet, originating from a bottom-quark. Also the neutrino reconstructed by using the missing transverse momentum. The two masses m_{top}^{pole} and m_{top} are close to each other with a possible difference of 1 GeV [9, 10].

The results of different measurements of m_{top} by ATLAS and CMS at the LHC, are summarized in Fig. (2.6). With the world average value combined from the four experiments ATLAS and CMS (LHC), CDF and Dϕ (TEVATRON) performed in March 2014

$$\mathbf{m_{top} = [173.34 \pm 0.36(stat.) \pm 0.67(syst.)]GeV}$$

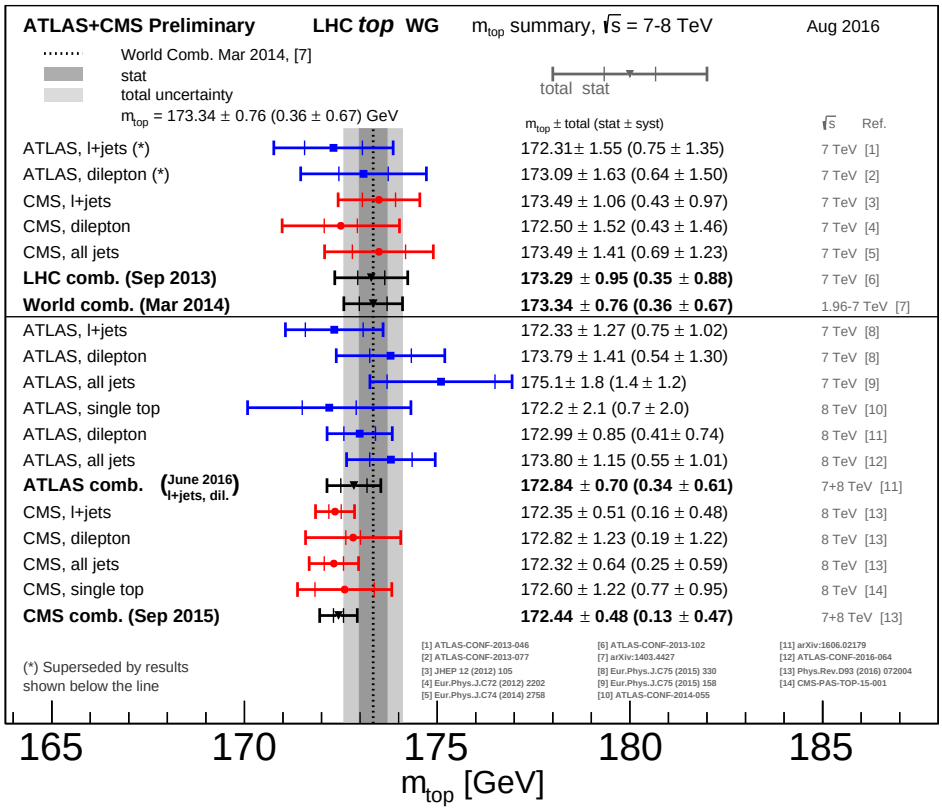

Figure 2.6: The top quark mass value obtained from the combined result of the ATLAS and CMS (LHC) [11].

2.3.1 Motivation for the top quark mass measurements

The top quark mass is a fundamental property of the top quark and due to its large value, it plays an important role in the Standard Model. Especially in the following aspects:

- **Vacuum stability:** the top quark mass (m_{top}) and the Higgs boson mass (m_H) are the most important parameters for electroweak vacuum stability studies, since they correspond to the maximum value of the gauge couplings allowed by vacuum metastability. The experimental values of m_{top} and m_H lie at the border between the stability and the metastability region of the SM vacuum, illustrated in Fig. (2.7), where a small change in the measured values of m_{top} and m_H can modify the conclusion a bout the vacuum stability. More details available in Ref. [12, 13].

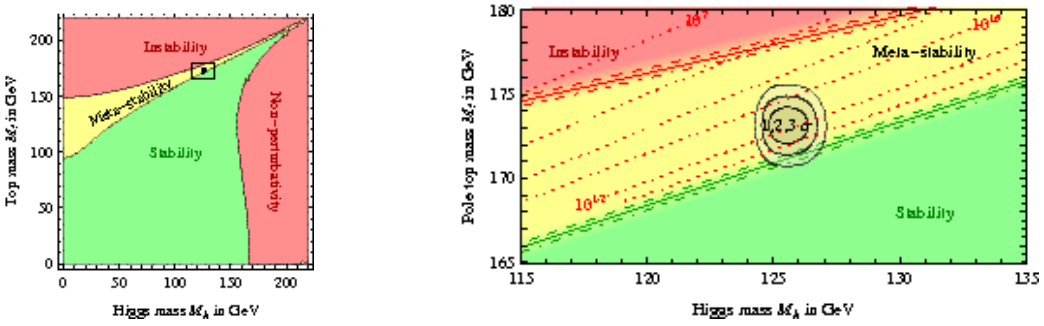

(a) (b)

Figure 2.7: SM vacuum phase diagram showing different regions: absolute stability, meta-stability and instability of the SM vacuum, and non-perturbativity of the Higgs quartic coupling. (b) Zoom in the region of the preferred experimental range of m_{top} and m_H where the allowed uncertainties at 1, 2 and 3σ are represented by the gray area [13].

- **EWSB and BSM:** the top quark mass plays a crucial role in the electroweak symmetry breaking (EWSB) and BSM sectors. Since it is the heaviest elementary particle it has the strongest Yukawa coupling (λ) with the Higgs boson. As a result the top quark represents an ideal laboratory for Higgs boson studies, as the stability of the Higgs potential, and Higgs boson propagator loop corrections, Fig. (2.8) (b)

shows the loops generated by the top-quark.

$$m_H^2 = m_H^2(LO) + \Delta m_H^2 \quad \text{with} \quad \Delta m_H^2 = -\frac{3\lambda_t^2 \Lambda_{UV}^2}{8\pi^2} + ... \tag{2.1}$$

Eq. (2.1) shows the squared leading order (LO) Higgs boson mass in addition to some correction, where λ_t is the top quark Yukawa coupling, and Λ_{UV} is ultraviolet momentum cutoff which is explained as the energy scale at which new physics (NP) appears. The strong dependence of the Higgs mass on a possible new scale is not explained by the SM symmetry and it is known as the hierarchy problem.

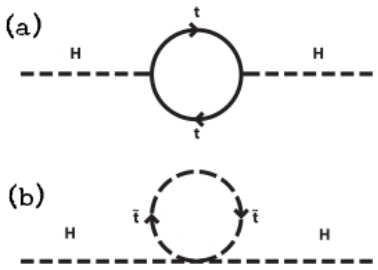

Figure 2.8: Feynman diagram shows the cancellation of the Higgs boson quadratic mass between top quark loop and stop squark tadpole in SUSY [14].

Different solutions are proposed by the BSM theories to solve the hierarchy problem, one of them is supersymmetry (SUSY), which predicts a new set of elementary particles called superpartners. Each fermion in the SM should have a partner boson, and each boson should have a partner fermion. By adding the stop correction to Eq. (2.1) it becomes:

$$m_H^2 = m_H^2(LO) + \Delta m_H^2 + \Delta m_H^2(stop) \quad \text{with} \tag{2.2a}$$

$$\Delta m_H^2(stop) = \frac{\lambda_{stop}^2}{16\pi^2}[\Lambda_{UV}^2 - 2m_{stop} \ln \frac{\Lambda_{UV}}{m_{stop}} + ...] \tag{2.2b}$$

Where λ_{stop} is the stop quark Yukawa coupling, and m_{stop} is its mass, Fig. (2.8) (b) shows the loops generated by stop.

- **Production mechanism of the Higgs boson:** the dominant production mechanism for the Higgs boson at the LHC, is the gluon-gluon fusion mediated by a virtual top quark loop. As a result precise measurement to the top-quark mass can lead to a better understanding of the production of the Higgs boson mechanism.

- **Test SM validity and constraint NP scenarios:** test the overall consistency of the SM through precise electroweak fit. Fig. (2.9) shows a scan of the confidence level profile of W boson mass m_W versus m_{top}. Both contours agree with the direct measurements shown in green. More details available in Ref. [15].

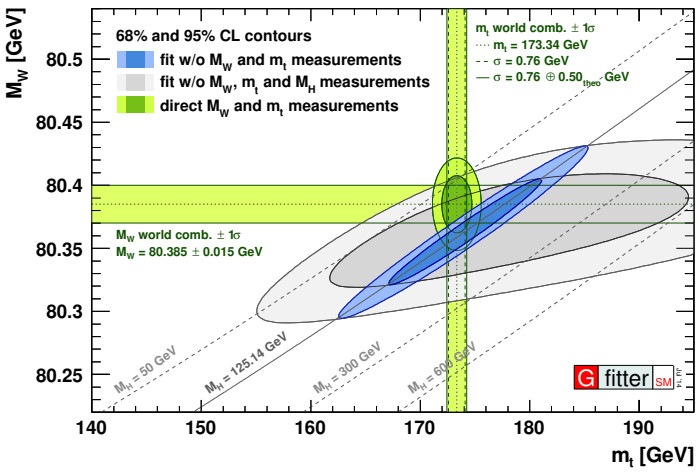

Figure 2.9: Scan of fits with fixed variables m_W vs. m_{top}. The result of the fit are: in blue including the m_H allowed region, in gray excluding m_H allowed region. The green bands and ellipse for the m_W and m_{top} direct measurements within 1σ [15].

2.3.2 The template method to measure the top quark mass

There are different techniques to measure the top quark mass. These include the matrix element, ideogram, template method and others. In this analysis we are using the template method for measuring the single top quark mass in the t-channel. This method has been used different times for measuring the top quark mass [16–19].

The template method's main idea is to get a simulated template distribution for a variable sensitive to the top quark mass (m_{top}) for discrete values of input m_{top}. These templates are fitted to a function that interpolates between the different input m_{top} values, while fixing the other parameters of the function. The final step to obtain the measured value of m_{top} is to apply a likelihood (LL) fit to the observed data distribution, 2.11 summarize these steps.

Fig. (2.10) shows a sketch that explains the simulated distributions of a variable sensitive to m_{top}. Using $O(m_{top})$ as a dummy variable sensitive to m_{top}.

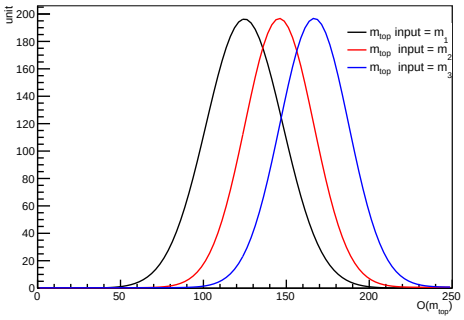

Figure 2.10: Sketch of templates of a variable $O(m_{top})$ which show a mass dependence. This variable has different distributions for different input m_{top}.

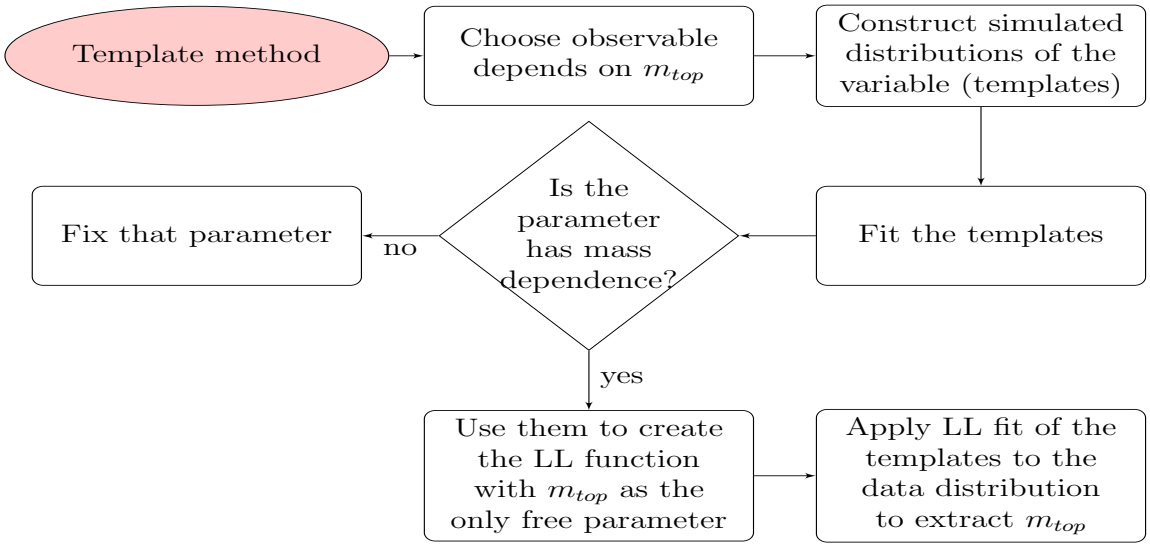

Figure 2.11: The template method steps to extract m_{top}.

Chapter 3

LHC and the ATLAS Detector

The **L**arge **H**adron **C**ollider (**LHC**) is the largest particle accelerator in the world. It is located at the Swiss-French border, and was built by the Euoropean Organization for Nuclear Research (**CERN**).

The LHC is a proton-proton and Pb-Pb collider. It is designed for a maximum center-of-mass energy of 14 TeV, and an instantaneous luminosity of $10^{34} cm^{-2} s^{-1}$. The main purpose of the LHC is to test the predictions of different theories of particle physics, such as measuring properties of the Higgs boson, searching for new particles predicted by BSM theories, and ansewring other unsolved questions of physics.

It is built in a circular tunnel of 27 km circumference, 100 m underground with four main interaction points. At each of these interaction points there is an experiment to detect particles produced from the interaction. These four detectors or experiments are: ATLAS, CMS, LHCb and ALICE. In addition to these four main experiments there are also three smaller experiments called: LHCf, TOTEM and MoEDAL. Fig. (3.1) shows a scheme of the LHC including the four experiments and the SPS (Super Proton Synchrotron), which is a pre-accelerator that injects the particles into the LHC ring.

One of the most important LHC parameters is the instantaneous luminosity, defined as the number of interactions per area and time and given by Eq. (3.1)

$$\mathscr{L} = \frac{\gamma}{4\pi} \frac{N_b^2 n_b f_{\text{rev}}}{\epsilon_n \beta^*} F \tag{3.1}$$

where γ is the relativistic Lorentz factor, N_b is the number of protons per bunch, n_b is the number of bunches per beam and f_{rev} is the revolution fre-

quency of the protons circulating in the accelerator. ϵ_n is the normalized transverse beam emittance, β^*[1] is the value of the beta function at the collision point and F is the geometric luminosity reduction factor. An overview of the LHC parameters are shown in Table 3.1.

Table 3.1: Comparison of the LHC parameters during the 2015 operation and the design values [20].

LHC Parameter	**Value in 2015**	**Design value**
Beam energy (TeV)	6.5	7
Protons/bunch ($10^{11}p$)	1.1	1.15
Bunch spacing (ns)	25	25
Max. number of bunch/beam	2244	2808
β^*(m)	0.8	0.55
Peak luminosity ($10^{34}cm^{-2}s^{-2}$)	0.51	1.0

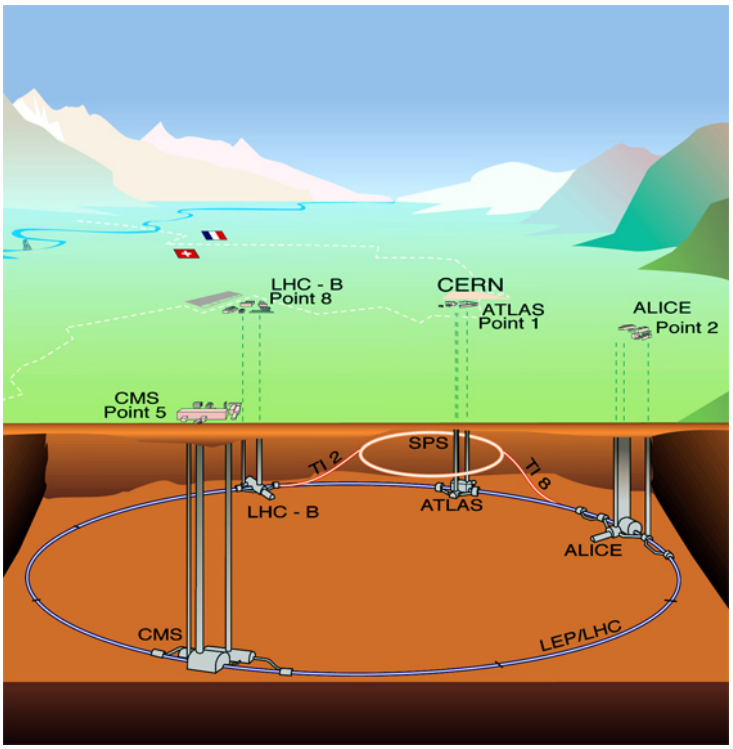

Figure 3.1: Overall view of the LHC four experiments [21].

[1]The beta function is a function related to the transverse particle beam size, where smaller beta means narrower beam size, and larger beta a broader beam.

In this thesis the data was collected by the ATLAS experiment, so the next section will describe it in more detail.

3.1 The ATLAS detector

A **T**oroidal **L**HC **A**pparatu**S** (ATLAS) is the largest detector at the LHC: 25 m in diameter, 44 m in length and with a weight of 7000 tons. It is built symmetrically around the interaction point, with different layers of sub-detectors. Fig. (3.2) shows an overview of the ATLAS experiment.

It is a multi-purpose detector, with a top priority of searching for the standard model Higgs boson, which was discovered by ATLAS and CMS in 2012. ATLAS also searches for supersymmetric particles, dark matter, extra dimensions and other predictions of BSM theories.

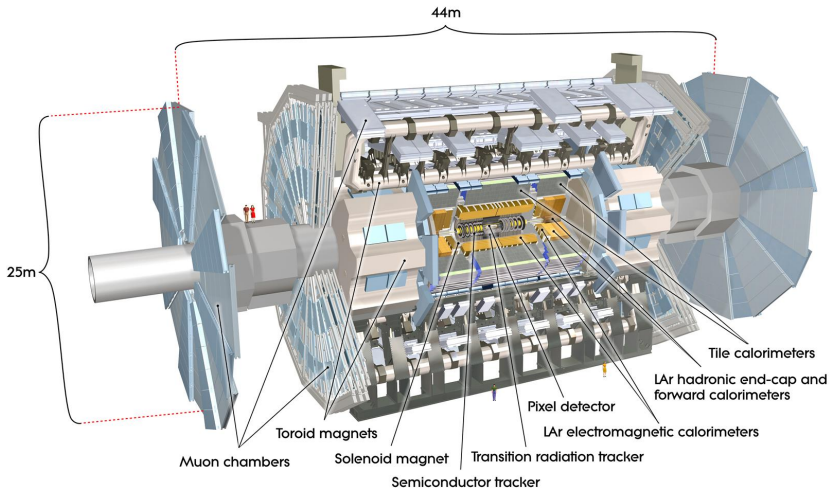

Figure 3.2: Overview of the ATLAS detector [22].

The ATLAS detector's coordinate system is right-handed (illustrated in Fig. (3.3)), and has the origin at the interaction point. The positive x-axis points from the interaction point toward the center of the LHC, the y-axis upwards and the z-axis in the beam direction. The azimuthal angle ϕ ranges from $-\pi$ to π in the x-y plane and is defined with respect to the positive x-axis. θ is the polar angle towards the positive z-axis. Typically, a different set of coordinates is used: the pseudo-rapidity definde as the angle of the

particle relative to the beam axis and given by:

$$\eta = -\ln[\tan\frac{\theta}{2}] \tag{3.2}$$

The distance in pseudo-rapidity-azimuth space:

$$\Delta R = \sqrt{\Delta\eta^2 + \Delta\phi^2} \tag{3.3}$$

The absolute value of the transverse momentum:

$$p_T = \sqrt{p_x^2 + p_y^2} \tag{3.4}$$

The transverse energy:

$$E_T = E\sin\theta \tag{3.5}$$

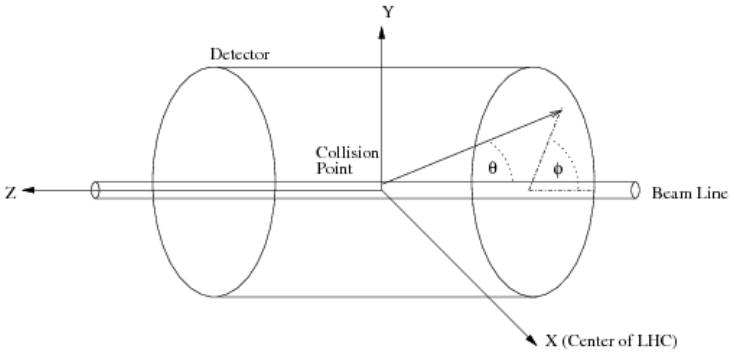

Figure 3.3: ATLAS detector coordinate system [23].

The ATLAS detector consists of different sub-detectors. The one closest to the interaction point is the Inner Detector (ID), followed by the Electromagnetic and Hadronic Calorimeters, while the outermost sub-detector is the Muon Spectrometer, as shown in Fig. (3.2).

3.1.1 The inner (tracking) detector

The inner detector (ID) is the innermost sub-detector in ATLAS, illustrated in Fig. (3.4), located in a magnetic field of 2 T generated by a solenoidal magnet surrounding the ID. It has a length of 6.2 m, outer radius of 1.05 m and covers a pseudo-rapidity range $\eta \leq 2.5$. The main purpose of the ID is

to reconstruct the trajectories of **charged** particles in order to measure their position and momentum. In addition, it is used to reconstruct vertices.

The ID consist of three sub-detectors: the innermost one is the Silicon Pixel detector, followed by the Semiconductor Tracker (SCT) and the Transition Radiation Tracker (TRT), as illustrated in Fig. (3.4). Each of these sub-detectors consist of a barrel and end-cap region.

The Silicon Pixel detector is the closest to the interaction point, consisting of three barrel cylinders and three discs in each end-cap. It is made of 1744 modules with 80 million pixel cells in total. Its main purpose is the identification and reconstruction of vertices and jets originating from short-lived particles such as b-hadrons and τ leptons.

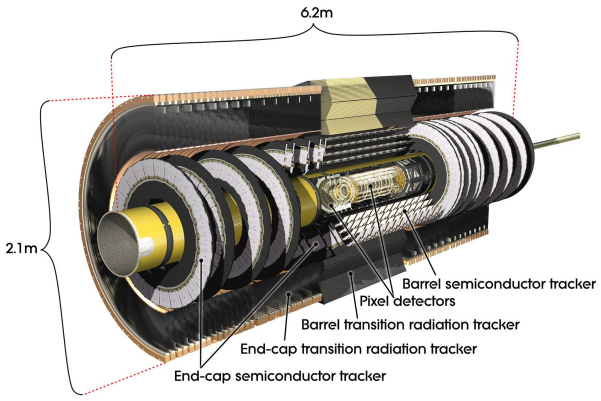

Figure 3.4: ATLAS Inner Detector [24].

The Semiconductor Tracker (SCT) is similar to the pixel detector, but consists of silicon strips sensors instead of pixel sensors. It is designed to measure eight space points per track, impact parameters and track momentum, as well as vertex positions.

The outermost layer is the Transition Radiation Tracker (TRT), consisting of straw tubes filled with a xenon gas mixture, which is ionized if a charged particle passes through it. It measures the transition radiation of these charged particles which helps to distinguish electrons from charged pions and improves the reconstruction of the tracks.

3.1.2 Calorimeters

The calorimeter system consists of the inner electromagnetic calorimeter (EM) and the outer hadronic calorimeter (HCAL), as shown in Fig. (3.5). The EM's purpose is to measure the energy of electrons and photons, while the HCAL measures the energy of hadrons and jets.

The electromagnetic lead liquid-argon sampling calorimeter (LAr)consists of three parts: the barrel, two end-caps and two forward calorimeters. It measures energy depositions of both photons and electrons, which produce electromagnetic showers in the absorber material. Photons produce $e + e-$ pairs when interacting with the material, while electrons radiate photons (Bremsstrahlung), estimates the pseudo-rapidity and direction of photons, reconstructs the position of electromagnetic showers, and measures the energy of the EM showers.

The hadronic calorimeter also consists of three regions: the tile calorimeter (includes tile barrel and tile extended barrel) and the end-cap. It provides a good energy resolution for the reconstruction of jets and missing transverse momentum.

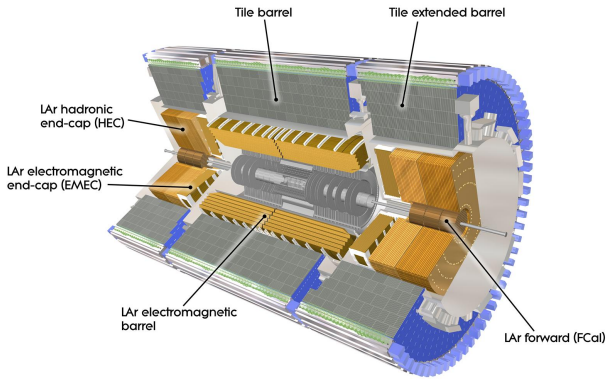

Figure 3.5: ATLAS Calorimeter system [25].

3.1.3 The muon spectrometer

The muon spectrometer is designed to detect muons and measure their momentum. It is situated within a large barrel toroidal magnet and two additional end-cap toroids which provide a magnetic field of 6T/m. The muon

detector consists of four muon chambers as shown in Fig. (3.6).

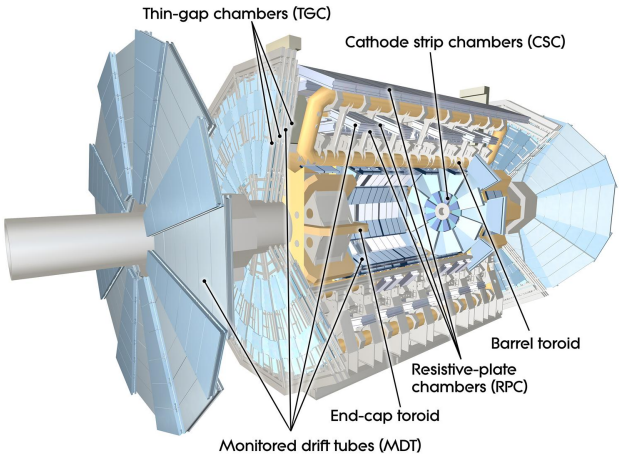

Figure 3.6: ATLAS Muon Spectrometer [26].

Chapter 4

Monte Carlo Simulations

Monte Carlo (MC) generators are computer simulation programmes that can produce hadron interactions according to the probability density of phase space and the matrix element of a given process. They play a very important role in particle physics in the context of evaluating systematic uncertainties and providing theoretical predictions.

The simulation of events happens in different stages. After the generation of the hard interaction by analytical perturbative calculation with leading order (LO) or next to leading order (NLO) precision, the parton showering and hadronization are simulated, then the interactions between the particles and the detector material are simulated followed by the digitalization in order to predict the detector response. The last step is the reconstruction of the signals using the same algorithms and techniques which are used for the reconstruction of observed events. This step is explained in Chapter 5.

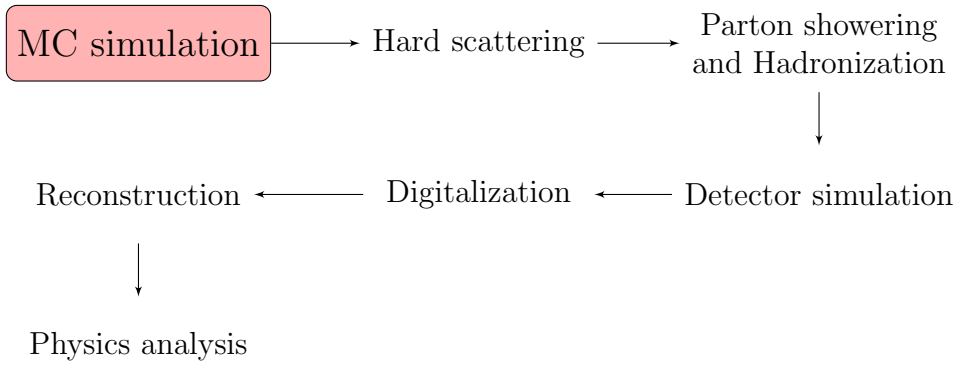

Figure 4.1: Monte Carlo simulated events generation process.

4.1 Event generation

The generation of the simulated events includes different stages, shown in Fig. (4.2):

- **Hard process:** The colliding partons are chosen according to the Parton Distribution Functions (PDFs) and the cross-section of the simulated processes, which depends on the matrix elements and the phase space. The matrix elements are calculated to LO or NLO precision depending on the process itself and the available generator.

- **Parton shower:** Particles produced from the hard process cause a secondary particles shower. Gluons are emitted from the initial or final states, which is referred to as initial and final state radiation (ISR/FSR). Higher order corrections are taken into ccount causing further radiation and parton multiplication.

- **Hadronization:** Resulting partons with a small distance in phase space and low energy are then grouped together into color-singlet hadrons.

- **Hadron decay:** Unstable hadrons decay into long-lived particles.

- **The underlying event:** Events resulting from the interaction of hadrons other than the ones contributing in the hard process.

- **Pileup:** Events resulting from the interaction of other protons in the same bunch, and initial/final state radiation (ISR/FSR) are additionally simulated and added. Ref. [27] includes more details about each stage.

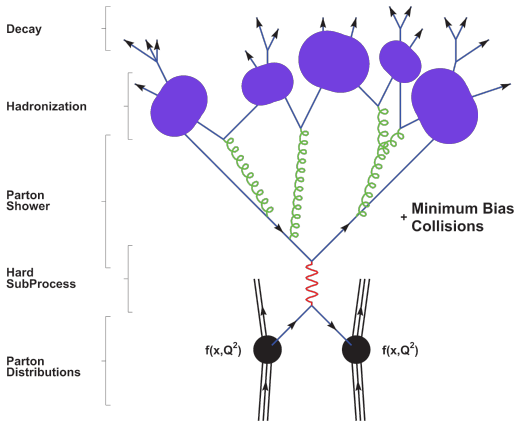

Figure 4.2: The basic structure of a hard hadron scattering MC event [28].

4.1.1 Monte Carlo generators

Two main types of MC generators are available: Matrix element (ME) generators and multi-purpose (MP) generators. The ME generators are used to simulate the hard process of the event generation, while the MP are used for the hard process, the showering, the hadronization and the hadron decay. In order to simulate the full event, combinations between ME and MP generators are applied.

Many Monte Carlo generators are available by now, and more are under developement. They differ with respect to their simulation scope, precision of the perturbative calculations, matching and merging of parton showers and the hard scatterings, and other aspects. In the following, MC generators used for this analysis are briefly described.

- **PowHeg-Box:** The **P**ositive **W**eight **H**ardest **E**mission **G**enerator is a ME generator that calculates the matrix elements to next-to-leading order (NLO) precision. In this analysis it is used to calculate the ME for the signal processes listed in Table 4.1. More details available in Ref. [29].

- **Pythia (version 6.4.27):** This is a MP generator that calculates the matrix elements to leading order (LO) precision. In this analysis it is used in combination with PowHeg for the ME calculations and to

simulate the parton showering for the signal processes generated with PowHeg. More details available in Ref. [30].

- **Sherpa:** **S**imulation for **H**igh **E**nergy **R**eactions of **PA**rticles is a MP generator. calculating the matrix elements to leading order (LO) precision. In this analysis it is used to generate the W+jets, the Z+jets and the diboson samples. More details available in Ref. [31].

- **Herwig (version 7.0.4):** This is a MP generator, simulating all the interactions except the underlying events, calculating the matrix elements to next-to-leading order (NLO) precision. In this analysis it is used for the signal shower systematic uncertainties calculations, combined with Pythia. More details available in Ref. [32].

- **aMC@NLO:** This is a ME generator that simulates all the interactions except the underlying events, calculating the matrix elements to next-to-leading order (NLO) precision. In this analysis it is used for the signal NLO matching systematic uncertainties calculations, combined with Herwig. More details available in Ref. [33].

4.1.2 Monte Carlo Samples

In this analysis a set of MC samples is used as shown in Table 4.1 for the signal samples. For the background processes, diboson samples can be found in Table 4.2, W+jets samples are shown in Table 4.3, while Z+jets samples are presented in Table 4.4. The table include the generator used, process ID, cross-section (σ) and the K-factor[2] for each sample.

[2]The K-factor is a higher order of the cross-section.

Table 4.1: signal MC samples used in this analysis [34, 35].

Process	**Generator**	**Dataset ID**	σ[pb]	**K-factor** [pb]
t-channel top quark	Powheg + Pythia	410011	43.739	1.0094
t-channel anti-top quark	Powheg + Pythia	410012	25.778	1.0193
s-channel top quark	Powheg + Pythia	410025	2.0517	1.0046
s-channel anti-top quark	Powheg + Pythia	410026	1.2615	1.0215
Wt-channel top quark	Powheg + Pythia	410013	34.009	1.054
Wt-channel anti-top quark	Powheg + Pythia	410014	33.989	1.054
$t\bar{t}$	Powheg + Pythia	410000	696.11	1.195

Table 4.2: Diboson MC samples used in this analysis [36].

Process	**Generator**	**Dataset ID**	σ[pb]	**K-factor** [pb]
$W^+ + W^- \rightarrow l\nu + qq$	Sherpa	361081	25.995	0.91
$W^+ + W^- \rightarrow qq + l\nu$	Sherpa	361082	25.974	0.91
$W + Z \rightarrow l\nu + qq$	Sherpa	361083	12.543	0.91
$W + Z \rightarrow qq + ll$	Sherpa	361084	3.7583	0.91
$Z + Z \rightarrow qq + ll$	Sherpa	361086	16.59	0.91

Table 4.3: W+jets MC samples used in this analysis [37–39].

Process	**Generator**	**Dataset ID**	σ[pb]	**K-factor** [pb]
$W \to e\nu$	Sherpa	361300	21283.0	0.9082
$W \to e\nu$	Sherpa	361301	21381.0	0.9082
$W \to e\nu$	Sherpa	361302	21385.0	0.9082
$W \to e\nu$	Sherpa	361303	633.67	0.9082
$W \to e\nu$	Sherpa	361304	632.29	0.9082
$W \to e\nu$	Sherpa	361305	631.59	0.9082
$W \to e\nu$	Sherpa	361306	90.163	0.9082
$W \to e\nu$	Sherpa	361307	90.039	0.9082
$W \to e\nu$	Sherpa	361308	90.129	0.9082
$W \to \mu\nu$	Sherpa	361324	21392.0	0.9082
$W \to \mu\nu$	Sherpa	361325	21381.0	0.9082
$W \to \mu\nu$	Sherpa	361326	21363.0	0.9082
$W \to \mu\nu$	Sherpa	361327	634.1	0.9082
$W \to \mu\nu$	Sherpa	361328	632.54	0.9082
$W \to \mu\nu$	Sherpa	361329	632.79	0.9082
$W \to \mu\nu$	Sherpa	361330	89.868	0.9082
$W \to \mu\nu$	Sherpa	361331	90.077	0.9082
$W \to \mu\nu$	Sherpa	361332	90.204	0.9082
$W \to \tau\nu$	Sherpa	361348	21386.0	0.9082
$W \to \tau\nu$	Sherpa	361349	21378.0	0.9082
$W \to \tau\nu$	Sherpa	361350	21385.0	0.9082
$W \to \tau\nu$	Sherpa	361351	635.56	0.9082
$W \to \tau\nu$	Sherpa	361352	634.01	0.9082
$W \to \tau\nu$	Sherpa	361353	633.0	0.9082
$W \to \tau\nu$	Sherpa	361354	90.013	0.9082
$W \to \tau\nu$	Sherpa	361355	90.209	0.9082
$W \to \tau\nu$	Sherpa	361356	90.169	0.9082

Table 4.4: Z+jets MC samples used in this analysis [40–42].

Process	**Generator**	**Dataset ID**	σ[pb]	**K-factor** [pb]
$Z \to ee$	Sherpa	361372	2206.6	0.9012
$Z \to ee$	Sherpa	361373	2205.4	0.9012
$Z \to ee$	Sherpa	361374	2205.9	0.9012
$Z \to ee$	Sherpa	361375	75.852	0.9012
$Z \to ee$	Sherpa	361376	76.023	0.9012
$Z \to ee$	Sherpa	361377	76.095	0.9012
$Z \to ee$	Sherpa	361378	11.696	0.9012
$Z \to ee$	Sherpa	361379	11.502	0.9012
$Z \to ee$	Sherpa	361380	11.653	0.9012
$Z \to \mu\mu$	Sherpa	361396	2202.3	0.9012
$Z \to \mu\mu$	Sherpa	361397	2205.0	0.9012
$Z \to \mu\mu$	Sherpa	361398	2204.4	0.9012
$Z \to \mu\mu$	Sherpa	361399	75.904	0.9012
$Z \to \mu\mu$	Sherpa	361400	76.117	0.9012
$Z \to \mu\mu$	Sherpa	361401	76.107	0.9012
$Z \to \mu\mu$	Sherpa	361402	11.646	0.9012
$Z \to \mu\mu$	Sherpa	361403	11.661	0.9012
$Z \to \mu\mu$	Sherpa	361404	11.652	0.9012
$Z \to \tau\tau$	Sherpa	361420	2196.4	0.9012
$Z \to \tau\tau$	Sherpa	361421	2204.1	0.9012
$Z \to \tau\tau$	Sherpa	361422	2204.7	0.9012
$Z \to \tau\tau$	Sherpa	361423	76.468	0.9012
$Z \to \tau\tau$	Sherpa	361424	76.012	0.9012
$Z \to \tau\tau$	Sherpa	361425	65.654	0.9012
$Z \to \tau\tau$	Sherpa	361426	11.656	0.9012
$Z \to \tau\tau$	Sherpa	361427	11.61	0.9012
$Z \to \tau\tau$	Sherpa	361428	11.669	0.9012

4.2 Detector simulation

The detector simulation programme plays the role of the real detector, by simulating the interactions of the generated events with the detector material as well as the detector response in ATLAS, the detector simulation program is the GEANT4 particle simulation toolkit [43].

Chapter 5

Physics Objects Reconstruction

Objects reconstruction refers to the use of digital signals recorded by different parts of the detector (calorimeter, muon system, etc.) to identify and reconstruct the physics particles produced in the proton-proton collision. Fig. (5.1) shows the trajectories of different particles in the ATLAS experiment.

Single top quark events include several objects, namely: electrons, muons, jets induced by b-quarks and missing transverse momentum caused by neutrinos. In this section, the reconstruction of these objects is briefly described.

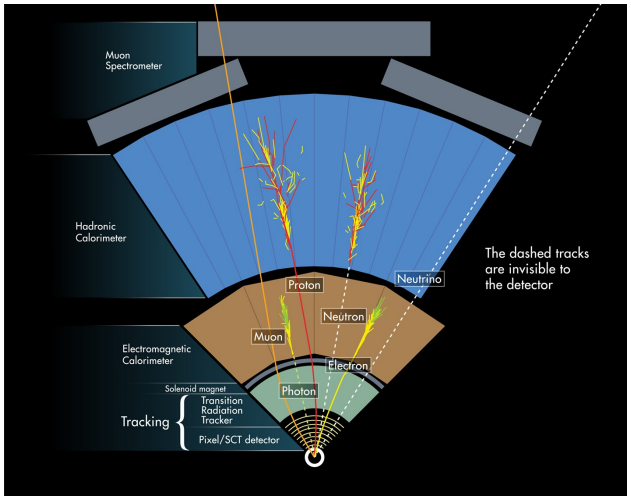

Figure 5.1: The trajectories of different particles in the ATLAS experiment [44].

5.1 Charged leptons reconstruction

The reconstruction of electrons is based on the identification of a set of energy clusters in the electromagnetic calorimeter (EM) and the information from the inner detector (ID). Since the electron is a charged particle, it leaves a track inside the ID and deposits its energy in the EM calorimeter due to bremsstrahlung.

In short, the electron candidates should have a transverse momentum $p_T > 25$ GeV, and pseudo-rapidity $|\eta|_{cluster} < 2.47$ GeV. More details available in Ref. [45].

The Muon reconstruction has three different approaches, named standalone, combined and tagged muon reconstruction, using the information from the Muon spectrometer (MS), ID and the calorimeters. Muons leave tracks in the ID and the MS. Similar to the electron, the muon candidates should have $p_T > 25$ GeV and pseudo-rapidity $|\eta| < 2.5$. More details available in Ref. [46].

5.2 Jets reconstruction

A jet is a group (spray) of many particles, produced by a high energy parton, and observed in the detector as a cluster of energy deposits in the hadronic calorimeter.

The reconstruction of jets uses the information from the calorimeters, where the deposited energy in the calorimeter cells has to be measured in a first step, followed by the jet reconstruction, using jet-finding algorithms, and finally the calibration of the energy of the jet. In addition, corrections have to be applied, such as energy corrections due to the pileup.

- **Energy measurements:** The energy clusters have to be constructed from the calorimeter cells. In ATLAS, the topological clusters approach is used, where the seed cells are calorimeter cells with alarge a mount of energy. Iteratively the nearest neighbour cells are added if their energy is above the noise level [47].
- **Jet reconstruction:** ATLAS uses the anti-k_T algorithm as the standard jet-finding algorithm. It belongs to the class of sequential recom-

bination algorithms, which start from calculating the distance between clusters and the distance between the cluster and the (LHC) beam and identify the smallest distance for each cluster. In case the distance between two clusters is the smallest, the two clusters are combined. If the distance between the i-th cluster and the beam is the smallest the i-th cluster is identified as a jet and removed from the cluster list. These steps are repeated untill all the clusters are included [48].

- **Jet calibration:** The final step of the jet reconstruction is to calibrate the energy of the jet, based on truth jets from MC simulated jet events.

5.2.1 *b*-jet reconstruction

In this analysis the *b*-jet reconstruction is important for the top-quark analysis. The B hadrons has a long lifetime ($\tau \approx 1.5$ ps) and relatively high mass and p_T, which allows us to distinguish it easily from other jets, using *b*-tagging algorithms. In this analysis the so-called MV2c algorithms are used. The MV2c algorithms use the output of the JetFitter, IP3D and SV1 algorithms as input. This is described in more detail in Ref. [49].

Fig. (5.2) shows a typical *b*-hadron decay, where the properties of the reconstructed secondary vertex allow the discrimination from light quark jets.

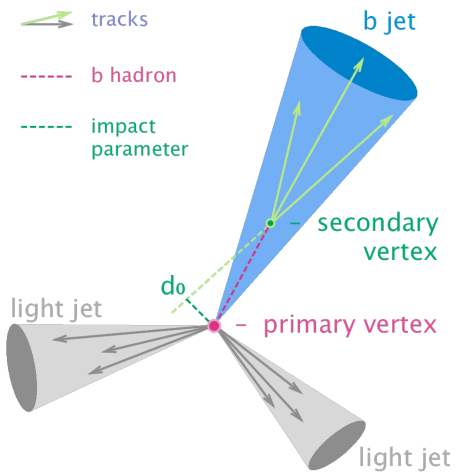

Figure 5.2: Schematic view of the *b*-hadron decay [50].

5.3 Missing transverse momentum reconstruction

Neutrinos cannot be measured directly by the ALAS detector, since they do not interact with the detector material. Their identification and reconstruction is done by measuring the missing transverse momentum E_T^{miss}. The transverse momentum in the ATLAS detector is conserved. As a result, if a momentum imbalance is measured, it indicates the presence of neutrinos.

The E_T^{miss} reconstruction depends on the energy deposited in the calorimeters and the muons reconstructed in the muon spectrometer (MS), as well as the correction of the energy loss in the cryostats between the EM and HCAL calorimeters [51].

The missing transverse momentum E_T^{miss} is defined as the negative vector sum of the momenta of all reconstructed objects:

$$\vec{E}_T^{miss} = -\sum_{rec.objects} \vec{P}_T \tag{5.1a}$$

$$E_T^{miss} = |\vec{E}_T^{miss}| \tag{5.1b}$$

The $\vec{E}_T^{miss}$ reconstruction includes the contributions from energy deposits in the calorimeters and the muon reconstruction.

$$\vec{E}_{x(y)}^{miss} = E_{x(y)}^{miss,calo.} + E_{x(y)}^{miss,\mu} \tag{5.2}$$

5.4 Top quark reconstruction

The top quark reconstruction depends on the reconstruction of its decay products, the b-tagged jet and the W boson. The four-momentum vector of the top quark is determined by adding up the four-momentum vector of the reconstructed b-tagged jet and the four-momentum vector of the reconstructed W-boson.

The four-momentum vector of the W-boson is given by $\vec{p}_W = \vec{p}_\ell + \vec{p}_\nu$, since the W-boson decays leptonically to a lepton and its corresponding neutrino. The momentum of the lepton is measured, while the neutrino momentum has to be extracted from E_T^{miss}. Additional information can be found in [52].

Chapter 6

Processes Description

6.1 The Dataset

The dataset used for this analysis is the one collected by the ATLAS detector at the LHC, between June and November 2015, at a center-of-mass energy ($\sqrt{s}$) of 13 TeV and a total integrated luminosity ($\mathscr{L}_{int}$) of 3.209 fb^{-1}.

Fig. (6.1) shows the total integrated luminosity versus time delivered by the LHC of 4.2 fb^{-1}, and the one recorded by ATLAS of 3.9 fb^{-1}. The dataset used for the physics analysis of 3.2 fb^{-1} differs from the recorded one, bacause not all the data satisfies the good data quality criteria, and all the reconstructed objects are of a good data quality.

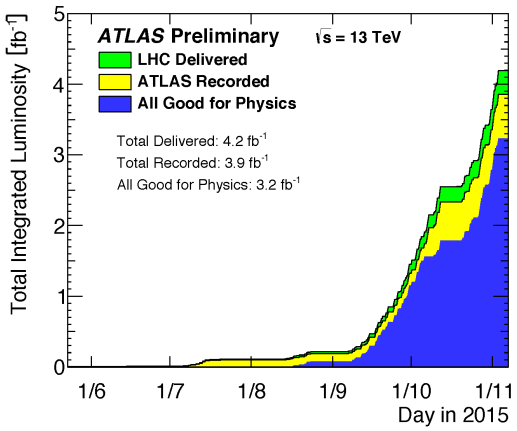

Figure 6.1: Total Integrated Luminosity between June and November 2015 [53].

6.2 Event selection

The selection of single top quark events produced in the t-channel is applied to data and simulated events, following the decay products of the process shown by the Feynman diagram in Fig. (2.5) which require: One charged lepton, electron or muon. Missing transverse energy E_T^{miss}. Exactly two jets, with one of them being b-tagged with 60% efficiency. Only the events that pass the **G**ood **R**un **L**ist (**GRL**) are selected, and each event is required to have one primary vertex at least.

Cuts on the selected leptons, jets, and missing energy are applied. The lepton is required to have $p_T > 30$ GeV and $|\eta| < 2.5$, $E_T^{miss} > 30$ GeV. While the two jets need to have $p_T > 35$ GeV and $|\eta| < 3.5$.

The leptons p_T cut is choosed to be greater than 30 GeV in order to reduce background with no leptons, like QCD background. For example the cut cannot be $p_T > 20$ GeV because of the trigger threshold, and cannot be high like 40 0r 50 GeV, because we lose so much signal. $|\eta| < 2.5$ is choosed to calibrate leptons much easiear. E_T^{miss} is required because of the neutrino in the decay products of the single top quark decay, and this helps to reduce Z+jets and QCD background. The two jets are required because the t-channel has two jets, one coming from the top quark decay and the other one from the associated production. $p_T > 35$ is a choice to optimize signal to background ratio. $|\eta| < 3.5$ is very important because the associated jet usually is a forward jet.

More cuts are applied in order to increase the fraction of the signal events contained in the selected event sample. A cut on the W boson transverse mass is applied $m_T(W) > 50$ GeV in order to reduce the multijet background events. Also a cut on the events with an additional lepton with $p_T > 10$ GeV is applied in order to reduce the di-lepton background events.

6.3 Signal processes

The signal processes includes all the processes that carrying information about the top quark mass:

- single top t-channel.

- single top s-channel.
- single top Wt-channel.
- $t\bar{t}$ pair.

6.4 Background processes

Background processes are those with similar decay products to the ones of the signal processes. The background processes usually, which will contaminate the signal processes.

- **W+jets:** is the most dominant background process in this analysis. It is associated with the production of W boson and additional jets. If the $W^{\pm}$ boson decays leptonically to a lepton and its corresponding neutrino, the final state products will be similar to the signal processes as shown in Fig. (6.2a), and passes the event selection.
- **Z+jets:** this process has a smaller contribution to the background processes than the W+jets. It is considered as a background process in case one of the leptons resulted from the Z boson detected is not detected as a lepton. The decay products are a Z boson and an additional jet, where the Z boson decays into two leptons (illustrated in Fig. (6.2b)).

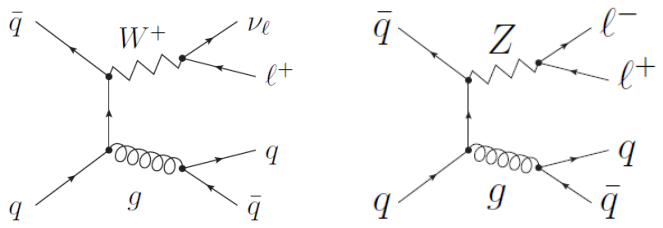

(a) (b)

Figure 6.2: Feynman diagrams of (a) W+jets, (b) Z+jets background processes [54].

- **Diboson:** this process also has a small contribution to the backgrounds. The decay products are two vector bosons: WW, or WZ, or

ZZ (illustrated in Fig. (6.3)). This process passes the event selection in case one of the bosons decays leptonically and the other hadronically.

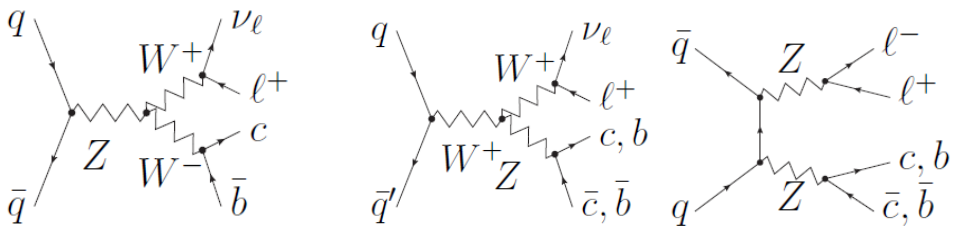

Figure 6.3: Feynman diagrams of the diboson background processes (a) WW, (b) WZ, (c) ZZ [54].

- **QCD-multijet:** It is the production of multijets from quantum chromodynamic interactions (illustrated in Fig. (6.4)). This process passes the event selection in case one of the produced jets is misidentified as a lepton, while there is enough missing transverse momentum.

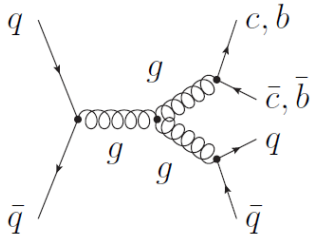

Figure 6.4: Example of a QCD-multijet background feynman diagram [54].

6.5 Signal and background discrimination

After describing the signal and the background processes in the previous sections, the signal events have to be separated from the background events in the observed dataset. For this purpose a multivariate technique is used, which is based on an artificial neural networks (NN) discussed more in this section. The NN results are used from the t-channel cross-section analysis [55].

6.5.1 Neural Network

An artificial neural network is inspired by the biological neural network. It consists of neurons (nodes) arranged in different layers, the layers are connected together by edges (synapses).

This analysis uses the NeuroBayes package which is a feed-forward NN, which consists of three layers as shown in Fig. (6.5). The first layer is called the input layer, the second is the hidden, while the third is the output layer. The first layer consists of 11 nodes for the 10 input variables plus one bias node. Each node in the input layer is connected with each node in the hidden layer. The hidden layer has 15 nodes, and all the hidden layer nodes are connected with the output node. The output layer consist of one node only O_{NN}.

The idea of a NN is to combine the discrimination power of the input variables and use the correlations between them to improve the separation between signal and background processes. That occurs in two main steps: preprocessing of the input variables and training of the NN.

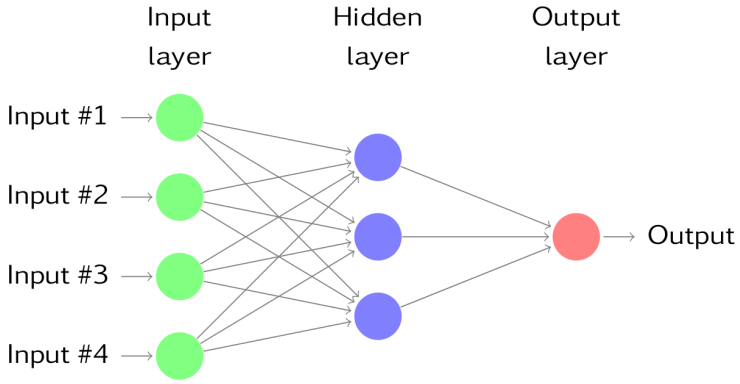

Figure 6.5: Schematic view of a three-layers feed-forward Neural Network [56].

- **Preprocessing of the input variables:** it is a step to prepare the input variables for the training in order to get a better starting point and increase the training speed. It includes individual preprocessing for each input variable and global preprocessing for all the variable.
- **Training of the NN:** to train the NN, samples are needed where the true category of an input event is known. The MC simulated samples for the signal and the background are used as the training dataset.

The signal process in the training is the t-channel single top-quark production. The background processes are $t\bar{t}$, Wt, s-channel and W+jets. QCD-multijet, Z+jet and diboson processes are not included in the training, because of their small contributions.

Fig. (6.6) shows the resulting NN output distribution. The shape distribution normalized to unit area for all the processes is shown in Fig. (6.6a), while the simulated and observed distribution is shown in Fig. (6.6b). Both of them show clearly that the t-channel single top peaks at higher values, while the two dominating background processes peak at lower values. So the NN output distribution separates well between signal and background processes.

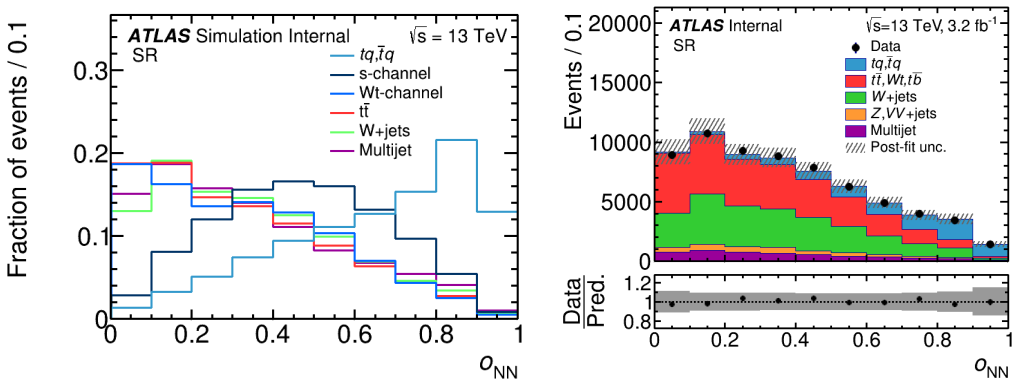

(a) (b)

Figure 6.6: The NN output distribution: (a) shape distribution normalized to unit area, (b) simulated and observed distribution.

6.5.2 Input variables

Ten different variables are used in the neural network training, summarized in table 6.1. These variables have the highest discrimination power between the t-channel events and the background. It includes the physics objects, lepton, missing transverse momentum and jets. Also, reconstructed particles like the W-boson and the top-quark. These include kinematic variables like p_T, η, invariant mass, and the angular distance ΔR between the measured and reconstructed particles.

Table 6.1: Input variables used in the NN training ordered by their discriminating power [55].

Variable	Definition
m($\ell\nu$b)	reconstructed top-quark mass from the charged lepton, neutrino and b-tagged jet.
m(jb)	invariant mass of the b-tagged and untagged jet.
$m_T(W)$	transverse mass of the reconstructed W boson.
$\eta(j)$	pseudo-rapidity of the untagged jet.
$m(\ell b)$	invariant mass of the charged lepton ℓ and the b-tagged jet.
$\eta(\ell\nu)$	rapidity of the reconstructed W boson.
$\Delta R(\ell\nu b, j)$	ΔR of the reconstructed top quark and the untagged jet.
$\cos\theta(\ell, j)$	cosine of the angle θ between the charged lepton and the untagged jet in the rest frame of the reconstructed top quark.
$\Delta p_T(\ell\nu b, j)$	Δp_T of the reconstructed top quark and the untagged jet.
$\Delta R(\ell, j)$	ΔR of the charged lepton and the untagged jet.

6.5.3 Cutting on the neural network output

In order to enhance the signal purity a cut on the neural network output $O_{NN} > 0.8$ is applied (illustrated in Fig. (6.6)). In Fig. (6.7) the contribution of each process is shown before and after applying the cut. It is clear that the dominating process changed from the $t\bar{t}$ process to the t-channel after the cut.

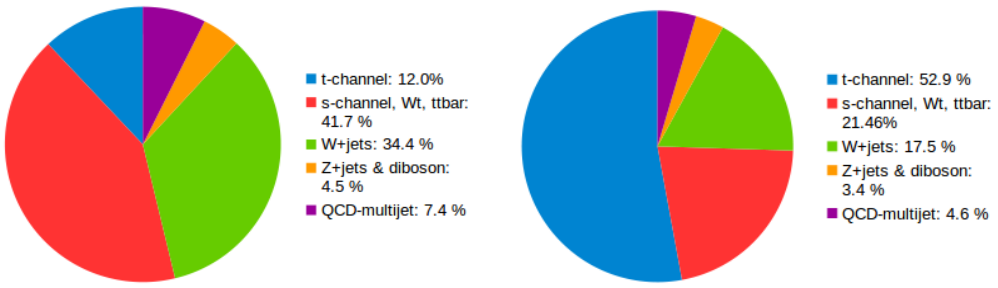

(a) (b)

Figure 6.7: Fraction of the different processes: (a) before the NN cut, (b) after the NN cut $O_{NN} > 0.8$.

6.5.4 Event yields

The event yields after the event selection and the NN output cut are summarized in Table 6.2 , for both the observed data and the expected simulated events.

Table 6.2: Event yields and the fraction after the cut on the NN output, for the expected and the data events.

Process	**Number of events**	**Fraction**
t-channel	2660	52.9%
s-channel, Wt, $t\bar{t}$	1089	21.6 %
W+jets	882	17.5 %
Z+jets and diboson	168	3.4%
QCD-multijet	232	4.6%
Total expected	5030	
Data	4839	

Chapter 7

Mass Measurements

In this chapter a mass measurement of single top-quark produced in the t-channel (m_{top}) is discussed. The methodology follows the first ATLAS mass measurement in a single top topology [19].

The template method introduced in section 2.3.2 is used for measuring m_{top} and discussed in more detail together with the evaluation of systematic and statistical uncertainties.

7.1 The template method

In the template method, simulated distributions or templates are constructed using MC dataset for a chosen variable sensitive to m_{top}, for three discrete input values of m_{top}. After that, these templates are fitted to a function that interpolate between the three different input values of m_{top}, fixing all other parameters of the function. Resulting in a fit function with m_{top} as the only free parameter. As a final step a binned maximum likelihood fit to the observed data distribution is used to extract the value of m_{top} that best describes the data. This procedure is explained in more detail in the following.

7.1.1 $m(\ell b)$ observable

In this analysis the chosen variable, sensitive to m_{top}, is the mass of the reconstructed lepton and b-jet $m(\ell b)$. This variable corresponds to the reconstructed top quark mass without contribution of the neutrino.

Fig. (7.1) shows the $m(\ell b)$ distribution after the NN output cut using simulated events for all the processes assuming $m_{top} = 172.5$ GeV: in blue the t-channel, in red the $t\bar{t}$, in green W+jets, orange Z+jets and diboson and the QCD-multijet distribution in violet. The observed data points are shown in black dots. Good agreement between the expected and the observed distributions are shown.

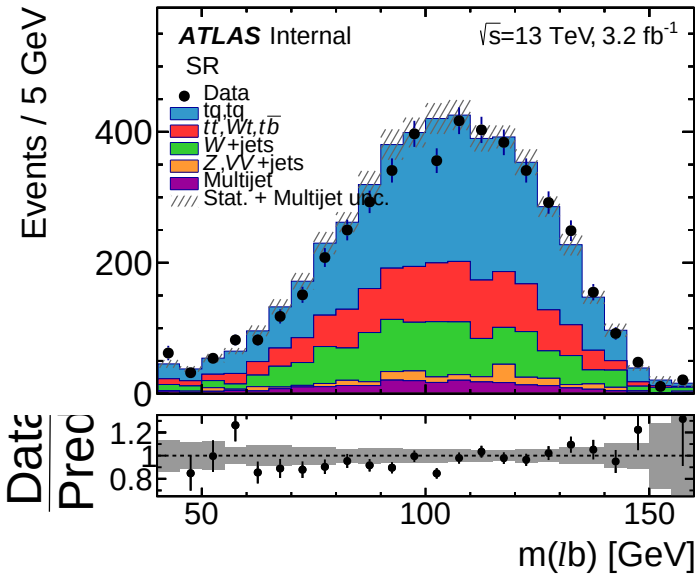

Figure 7.1: $m(\ell b)$ distribution after the NN output cut for the simulated signal and background processes. The black dots show the observed data.

7.1.2 Construction of the fitting templates

The fitting templates are constructed in three main steps:

1. Construct the $m(\ell b)$ distributions using MC samples, for three input mass points: 170, 172.5 and 175 GeV. The distribution corresponds

to 172.5 GeV mass is fitted with the sum of a Gaussian and Landau functions with seven parameters dependence given by:

$$f(p_0....p_6, x = m(lb)) = p_0 \cdot ((1 - p_1) \cdot G(x|p_5, p_6) + p_1 \cdot L(x|p_2, p_3, p_4)) \tag{7.1}$$

Where p_0 is the overall normalization, p_1 is the relative Gaussian and Landau fraction, p_2, p_3 and p_4 are the shift, mode and scale of landau respectively, p_5 and p_6 are the mean and width of the Gaussian function respectively.

2. Fix four of the parameters: the relative Gaussian and Landau fraction (p_1), the shift of Landau (p_2), the scale of landau (p_4) and the width of the Gaussian (p_6) are fixed to the result obtained from the fit of the template with m_{top} = 172.5 GeV since these parameters do not have any mass dependance.

3. Perform the fit for the templates of $m(\ell b)$ with the three mass points and obtain the mode of Landau (p_3) and the mean of Gaussian (p_5) in each case, since they have a linear dependence on m_{top} (verified later in this section).

The $m(\ell b)$ distributions are shown in Fig. (7.2) for the three input masses. The values for p_1, p_2 and p_4 are fixed to the values obtained from the fit to the distribution with m_{top} = 172.5 GeV. The values of each parameter for the three different mass points are summarized in Table 7.1.

Table 7.1: Parameters after fitting the $m(\ell b)$ distributions for the three input mass points: 170, 172.5, 175 GeV .

Parameter	**170 GeV**	**172.5 GeV**	**175 GeV**
p_0	978.36	965.44	924.10
p_1	fixed	0.77	fixed
p_2	fixed	154.24	fixed
p_3	37.24	35.75	34.79
p_4	fixed	11.83	fixed
p_5	100.74	101.63	103.29
p_6	fixed	20.78	fixed

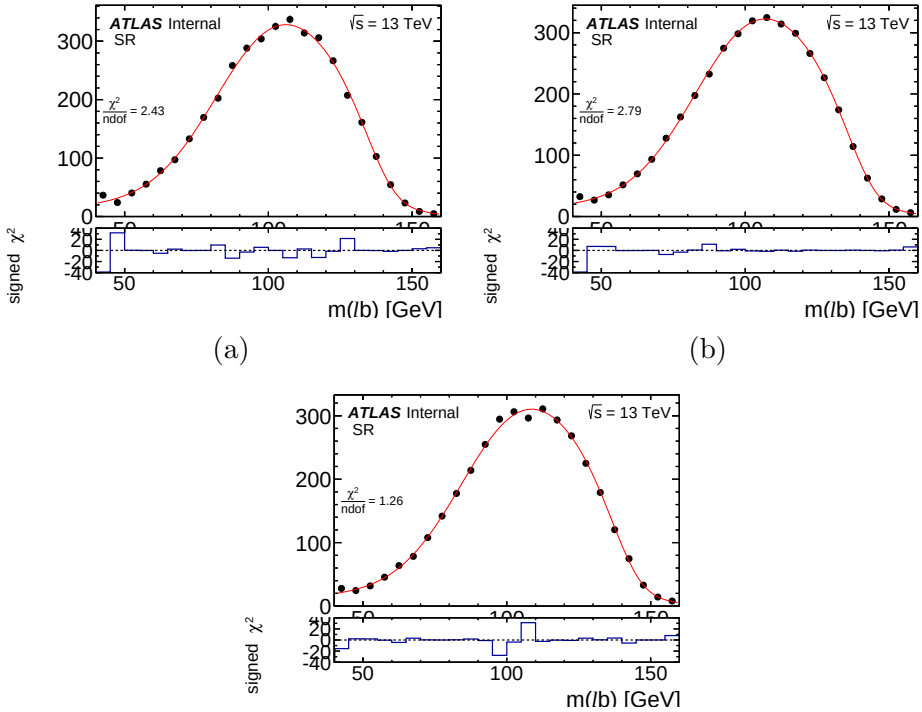

Figure 7.2: $m(\ell b)$ simulated signal distributions for different input masses : (a) 170 GeV (b) 172.5 GeV, (c) 175 GeV. Fitted to the function defined in Eq. (7.1).

7.1.3 Top quark mass dependence on $m(\ell b)$

Fig. (7.3) shows the linear dependence of p_3 and p_5 on the input m_{top} after applying a linear fit with:

$$p_i = p_0.m_{top} + p_1, \text{ with i = 3 or 5} \tag{7.2}$$

The mass dependence of these two parameters is shown exactly by Eq. (7.3), where p_0 and p_1 are obtained from the result of the fit in Fig. (7.3). As a result m_{top} is the only free parameter.

$$p_3 = -0.49 * m_{top} + 120.58 \tag{7.3a}$$

$$p_5 = 0.51 * m_{top} + 14.10 \tag{7.3b}$$

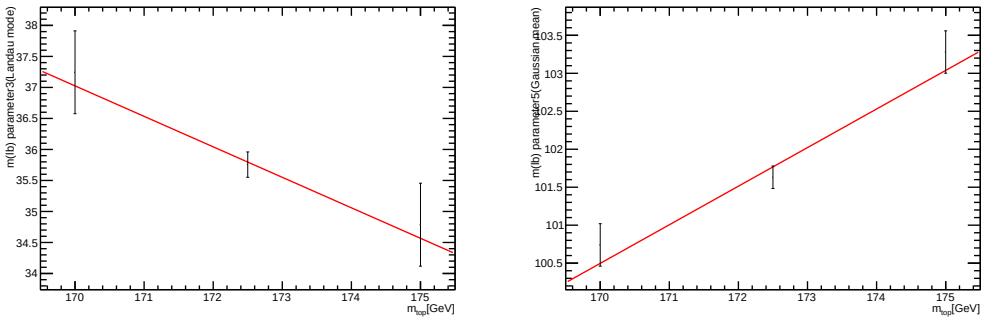

(a) (b)

Figure 7.3: Mass dependent parameters, fitted with Eq. (7.2): (a) Landau mode (p_3) (b) Gaussian mean (p_5).

7.1.4 Likelihood fit to extract m_{top}

Finally a binned maximum likelihood fit is performed to the template using the $m(\ell b)$ data distribution to extract m_{top}.

The likelihood function is built using the signal and background templates, given by Eq. (7.4). The first term includes the signal and background templates as well as the data distribution, while the second term is a Gaussian constraint on the background rates.

$$L(\beta^s, \beta^b_j) = \prod_{k=1}^{M} \frac{e^{-\mu_k} \cdot \mu_k^{nk}}{n_k\,!} \cdot \prod_{j=1}^{B} G(\beta^b_j; 1.0, \Delta_j), \qquad \text{with} \tag{7.4a}$$

$$\mu_k = \mu^s_k + \sum_{j=1}^{B} \mu^b_{jk}, \quad \mu^s_k = \beta^s \cdot \tilde{\nu_s} \cdot \alpha^s_k(m_{top}), \quad \text{and} \quad \mu^b_{jk} = \beta^b_j \cdot \tilde{\nu_j} \cdot \alpha_{jk} \tag{7.4b}$$

where j runs over the background processes and s over the signal processes, k is an index for the bin number; μ^s_k number of expected signal events in bin k, μ^b_{jk} number of expected background events in bin k, $\tilde{\nu}$ is the number of predicted events in the selected dataset for a certain process. B is the number of considered background processes and equal one. n_k the number of observed events in bin k. β^s scale factor for signal, β^b_j scale factor for backgrounds.

α_{jk} background template fraction, and $\alpha_k^s(m_{top})$ signal template fraction and have the mass dependence in the following way:

$$\alpha_k^s(m_{top}) = \frac{\int_{x_{min}(k)}^{x_{max}(k)} f(m_{top})}{\int_{k_i}^{k_f} f(m_{top})} \tag{7.5}$$

which is the integral of the function given in Eq. (7.1) using Eq. (7.3a) and Eq. (7.3b), for each bin over the integral from the first bin k_i to the last one k_f of the same function.

The second part of Eq. (7.4a) is the Gaussian function with mean equal to one, and a width Δ_j. More details about the Maximum likelihood fit can be found in Ref. [57].

An equivalent calculation to the maximum binned likelihood fit is performed. It is a minimization of the negative logarithm of the likelihood function using the MINUIT program [58].

Fig. (7.4) shows the $m(\ell b)$ distribution for the signal process, the W+jets background and the data. Fig. (7.4a) shows the simulated distribution using input mass 172.5 GeV compared to data, while Fig. (7.4b) using the result after performing the likelihood fit templates, The values of the scale factor β are shown for the signal and background processes. It is shown that the template are shifted to the right and more consistent with the data after using the likelihood fit results.

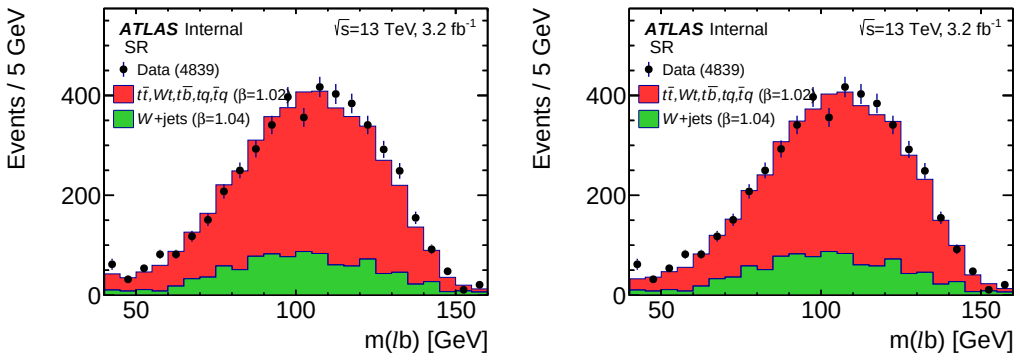

Figure 7.4: $m(\ell b)$ distribution for signal and background processes compared to data: (a) MC distribution with input mass 172.5 GeV compared to data, (b) fitted templates to the data after performing the binned maximum likelihood fit using the best fit of m_{top}.

7.2 Method validation

Ensembles of pseudo experiments are used in order to check the method, by creating a pseudo dataset from simulated distributions of the $m(\ell b)$ observable. After that, the binned maximum likelihood fit is applied to measure m_{top} in each pseudo dataset. Finally, the known input values of m_{top} are compared with the output of the pseudo experiments.

Pseudo dataset are created for three values of m_{top}: 170, 172.5 and 175 GeV, by drawing randomly a number of signal and background events for each pseudo dataset from the $m(\ell b)$ distribution, where the number of events is calculated using a Poisson distribution. This procedure can be repeated N times to generate N ensembles of pseudo experiment.

10000 ensembles of pseudo dataset are created for each of the three mass point, where larger number pseudo dataset ensembles helps to reduce the statistical uncertainties. Fig. (7.5) shows the mass distribution generated from the pseudo datasets for input $m_{top} = 170$, 172.5, and 175 GeV, and the mean value $\langle m_{top}^{out} \rangle$ of 169.903 GeV and 172.500 GeV, respectively.

Fig. (7.6) shows the top mass linearity plot (left), and the difference between the input mass and the output one ($m_{top} - \langle m_{top}^{out} \rangle$) as a function of the input value (right).

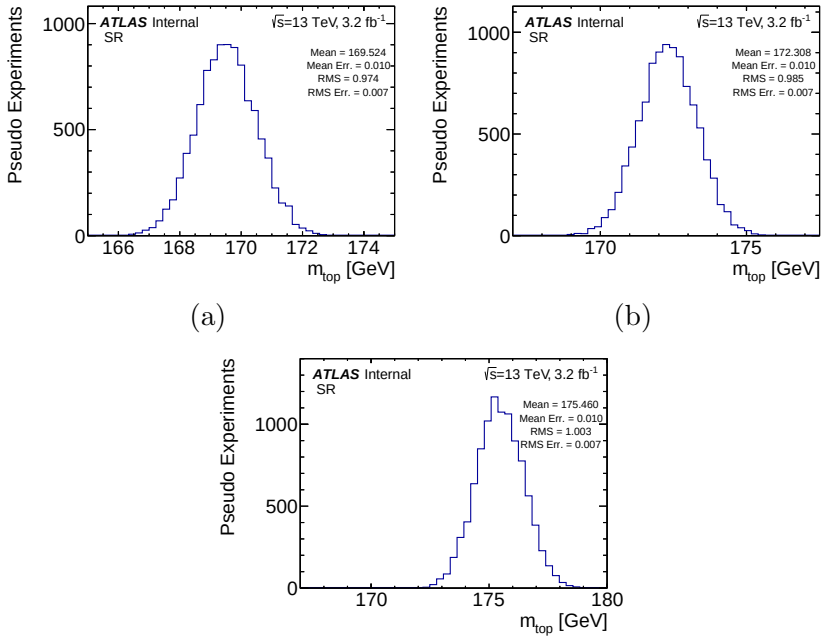

Figure 7.5: Mass distribution generated from the pseudo datasets for input m_{top}: (a) 170 GeV, (b) 172.5 GeV, (c) 175 GeV.

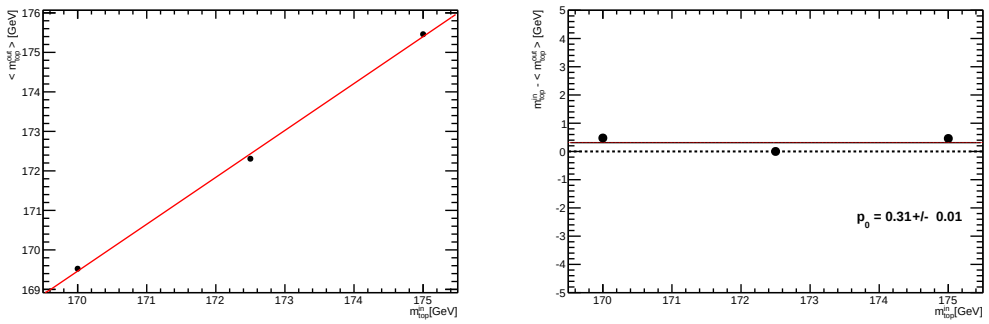

Figure 7.6: The x-axis shows m_{top} the used m_{top} in the simulation, the y-axis: (a) the output mass of pseudo experiments $\langle m_{top}^{out} \rangle$, (b) the difference $m_{top} - \langle m_{top}^{out} \rangle$.

7.3 Systematic uncertainties

Different systematic uncertainties affect the mass measurement. The most dominant ones will be calculated and explained in this section. These uncertainties are applied only to the signal processes (t-channel, s-channel, Wt-channel), $t\bar{t}$ and the W+jets background process.

Generating pseudo experiments are used to calculate the systematic uncertainties, by varying the source of uncertainties by one standard deviation ($\pm 1\sigma$) with respect to the nominal value. Then calculating the difference between $\langle m_{top}^{out,+1\sigma} \rangle$ or $\langle m_{top}^{out,-1\sigma} \rangle$ and the nominal value $\langle m_{top}^{out} \rangle$, illustrated in Fig. (7.9) for an example. The final total systematic uncertainty is calculated by summing each systematic contribution quadratically.

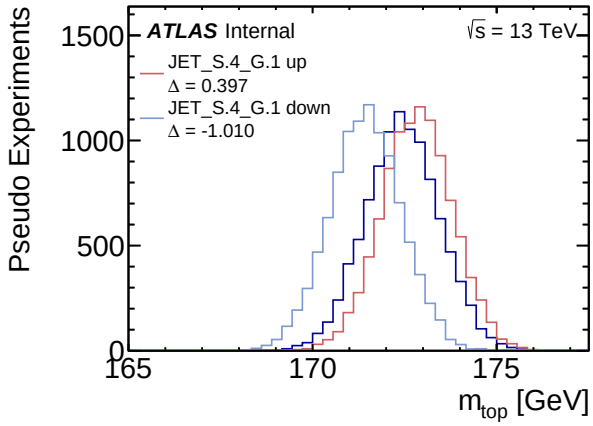

Figure 7.7: Example on how the systematic uncertainties are calculated. By varying the uncertainty source by $+1\sigma$ (red curve) and -1σ (light blue), where the nominal distribution in dark blue.

7.3.1 Object energy scale/resolution and efficiencies uncertainties

- **Jet energy scale (JES) uncertainty:** it is one of the most dominant uncertainties in the top-quark mass measurements, because of the direct relation between m_{top} and the jet energy. It is originating from a limited ability to reconstruct kinematic variables of the reconstructed jets with the ATLAS calorimeter system.

The JES uncertainty includes several components: residual JES correction factors, high-p_T extrapolation, intercalibration of jets at higher pseudo-rapidity, pileup, b-jet energy scale (bJES) and others. A detailed description can be found in [59].

- **Jet energy resolution (JER) uncertainty:** it is also due to the limited ability to measure the exact energy of the jets with the ATLAS calorimeter. The JER uncertainty is calculated by smearing the jet energy in the MC events to match the data by a Gaussian function depending on the jet p_T and η. Comparing the result of pseudo-experiments in case of the nominal energy resolution with the result in case of the smeared jet energy. A detailed description can be found in [60].

- **Missing transverse energy (E_T^{miss}):** it is reconstructed from the reconstructed jets, electrons and muons, as discussed in section 5.3. As a result the systematics uncertainties are propagated through the E_T^{miss} calculations accordingly.

  Different sources of systematic uncertainties contributes to the E_T^{miss} uncertainty: the cell-out uncertainty (scale and resolution), the soft-jet uncertainty (scale and resolution), the pileup uncertainty, and the liquid argon hole problem uncertainty. The cell-out and soft-jet uncertainties are correlated, while all the others are taken as uncorrelated [61, 62].

- **Lepton modelling uncertainties:** includes uncertainties on the identification efficiency, reconstruction efficiency, trigger efficiency and the lepton isolation are evaluated for both electrons and muons. By performing a correction scale factors to the MC events in order to get a better MC to data agreement. The uncertainty of the muon energy scale and resolution is considered as well [63].

- **b-tagging efficiency:** the uncertainty due to the efficiency of the the identification of the b-jets using the MV2c tagging algorithm is evaluated, using the technique described in Ref. [64].

Table 7.2 summarize the results of each of the uncertainty source discussed above.

Table 7.2: Systematic uncertainties due to objects energy scale or resolution and the efficiencies uncertainties

Source	**+ ve Δm_{top}[GeV]**	**- ve Δm_{top}[GeV]**
Jet energy scale (JES)	0.65	-1.04
Jet energy resolution (JER)	0.00	-0.62
E_T^{miss} scale	0.04	-0.13
E_T^{miss} resolution	0.02	-0.02
Lepton ID efficiency	0.02	-0.01
Lepton reconstruction efficiency	0.00	0.00
Lepton trigger efficiency	0.02	-0.01
Muon energy resolution	0.06	0.00
Muon energy scale	0.02	-0.02
b-tagging efficiency	0.05	-0.05

7.3.2 Pileup re-weighting uncertainty

The pileup events have to be considered and added to the simulated hard scattering events. In order to get a better data to MC agreement, by applying weights corrections to the simulated events in order to fit the simulated distribution to the data distribution. The pile up re-weight positive uncertainty is 0.73 GeV, while the negative value is -0.03 GeV. Fig. (7.8) shows the luminosity weighted distribution of the mean number of interactions per crossing.

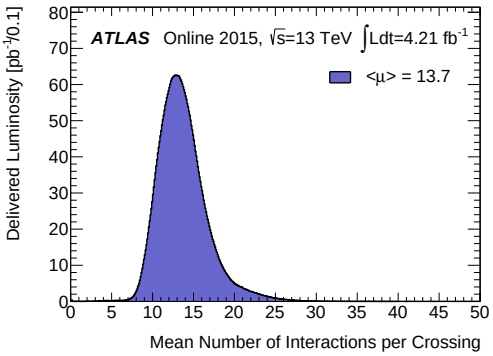

Figure 7.8: Number of interactions per crossing bunch. Data recorded in 2015 between 3 June till 3 November at $\sqrt{s} = 13$ TeV [65].

7.3.3 Simulation modelling uncertainties

- **Parton shower and NLO matching:**

  The parton shower uncertainty comes from the choice of the generators used for the parton shower during simulation. It is estimated for the $t\bar{t}$ production process and the t-channel signal process. By estimating the effect on $\langle m_{top}^{out} \rangle$ when using different generators for the event generation. PowHeg + Pythia6 are compared to PowHeg + Herwig7 and the full difference between the two cases is quoted as uncertainty.

  The NLO matching uncertainty is estimated the same way as the parton shower uncertainty, for both the $t\bar{t}$ and the t-channel processes, By comparing PowHeg + aMC@NLO and PowHeg + Herwig7 generators.

- **Initial and final state radiation:** the uncertainties due to the effect of the initial and final State radiation (ISR/FSR) is also calculated for both the $t\bar{t}$ and the t-channel processes. Using samples with modified scales in the MC calculations as well as the parton shower.

Table 7.3 summarize the results of each of the simulation modelling uncertainties discussed above.

Table 7.3: Systematic uncertainties due to simulation modelling.

Source	**+ ve** Δm_{top}**[GeV]**	**- ve** Δm_{top}**[GeV]**
t-channel parton shower	1.88	-2.27
$t\bar{t}$ shower	0.20	-0.21
t-channel NLO matching	0.61	-0.49
$t\bar{t}$ NLO matching	0.23	-0.23
t-channel radiation	0.14	-1.61
$t\bar{t}$ radiation	0.11	0.00

7.3.4 Backgrounds rate

The backgrounds rate systematic uncertainties are calculated for the W+jet,

diboson, Z+jet and the QCD multijet background processes. By shifting the rate of the background processes by one standard deviation up and down. The total background rate uncertainty is calculated by the quadratic sum of the individual background processes rate uncertainty, which is equal 0.17 GeV up and 0.17 GeV down.

7.3.5 Summary

Table 7.4 summarizes the systematic uncertainties affecting the top-quark produced in the t-channel mass measurement. The total uncertainty calculated by the quadretic sum of all the individual uncertainties. The most dominant uncertainties are: the jet energy scale, the pileup re-weighting and the t-channel modelling uncertainties.

Table 7.4: Summary of the systematic uncertainties.

Source	**+ ve Δm_{top}[GeV]**	**- ve Δm_{top}[GeV]**
Jet energy scale (JES)	0.65	-1.04
Jet energy resolution (JER)	0.00	-0.62
E_T^{miss} scale	0.04	-0.13
E_T^{miss} resolution	0.02	-0.02
Lepton ID efficiency	0.02	-0.01
Lepton reconstruction efficiency	0.00	0.00
Lepton trigger efficiency	0.02	-0.01
Muon energy resolution	0.06	0.00
Muon energy scale	0.02	-0.02
b-tagging efficiency	0.05	-0.05
pileup re-weighting	0.73	-0.03
t-channel shower	1.88	-2.27
$t\bar{t}$shower	0.20	-0.21
t-channel NLO matching	0.61	-0.49
$t\bar{t}$ NLO matching	0.23	-0.23
t-channel radiation(ISR/FSR)	0.14	-1.61
$t\bar{t}$ radiation(ISR/FSR)	0.11	0.00
Background rates	0.17	-0.17
Total systematic uncertainty	2.24	-3.11

7.4 Statistical uncertainty

The statistical uncertainty is also calculated using pseudo experiments in the same way described in section 7.2, which represents the root mean square (RMS) of the mass distribution shown in Fig. (7.9), and equal to 0.98 GeV.

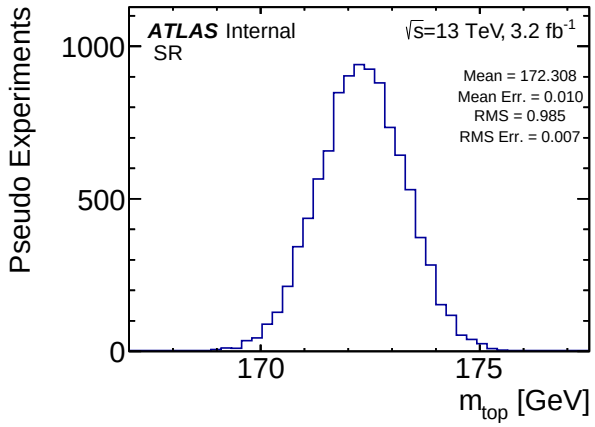

Figure 7.9: Mass distribution generated from the pseudo-datasets for m_{top} 172.5 GeV.

Chapter 8

Results and Conclusion

This thesis studied the template method to measure the single top quark mass in the t-channel with the ATLAS detector at the LHC. By applying it on 2015 dataset with a center of mass energy of 13 TeV and an integrated luminosity of 3.2 fb^{-1}.

Considering the statistical and systematic uncertainties the value of the top quark mass is measured to be:

$$\mathbf{m_{top} = [174.56 \pm 3.22(syst.) \pm 0.98(stat.)]\ GeV}$$

The given total systematic uncertainty correspond to the quadretic sum of the components listed in Table 8.1, with the most dominated uncertainties are the jet energy scale, the pileup re-weighting and the t-channel modelling systematic uncertainties.

Table 8.1: sources of the systematic uncertainties.

Source	$\lvert\Delta m_{top}\rvert$**[GeV]**
Jet energy scale (JES)	1.04
Jet energy resolution (JER)	0.62
E_T^{miss} scale	0.13
Lepton ID efficiency	0.07
Muon uncertainties	0.05
b-tagging efficiency	0.05
pileup re-weighting	0.73
Background rates	0.17
Simulation modelling	2.87
Total systematic uncertainty	3.22

The methodology of the presented measurement is built on a brevious measurement of the top quark mass with the ATLAS detector at a center of mass energy $\sqrt{s} = 8$ TeV, documented in Ref. [19], where the template method is used to extract the value of the top quark mass from the distribution of the invariant mass of the lepton and the b-jet ($m(\ell b)$). $m(\ell b)$ distributions are reconstructed using Monte Carlo samples generated with different settings of the top quark mass. A function depending on several parameters are fitted to the reconstructed distribution. The parameters are plotted as a function of m_{top} and fit is performed to parameterize the mass dependence of the parameters. Finally a binned maximum-likelihood fit is perforemed to the data distribution to extract the measured value of m_{top}.

Increasing the dataset to the one with higher luminosity as 36 fb^{-1} can help to reduce the statistical uncertainty, as shown in Fig. (8.1). Also the systematic uncertainties will be improved by more studies to the generator uncertainties, as well as increasing the dataset. The systematic uncertainties evaluated are only the preliminary ones.

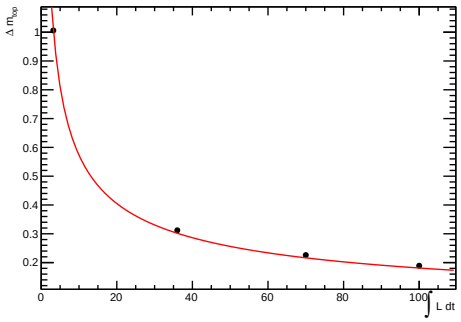

Figure 8.1: Statistical uncertainty for integrated luminosity values: 3.2, 36, 72 and 100 fb^{-1}.

The luminosity of 36.1 fb^{-1} was satisfied with 2015 and 2016 datasets, while the 100 fb^{-1} is expected to reach in the next two years, with 2015, 2016, 2017 and 2018 datasets.

Bibliography

[1] W.N. Cottingham, D. A. Greenwood, An Introduction to the Standard Model of Particle Physics, 2007.

[2] Jeroen van Tilburg home page, research, https://www.nikhef.nl/~jtilburg/img/SM.png, March, 2017.

[3] ATLAS Collaboration, Observation of a new particle in the search for the Standard Model Higgs boson with the ATLAS detector at the LHC, Phys. Lett. B716 (2012) pp. 1-29, arXiv:1207.7214v2 [hep-ex].

[4] CMS Collaboration, Observation of a new boson at a mass of 125 GeV with the CMS experiment at the LHC, Phys. Lett. B 716 (2012) 30, arXiv:1207.7235v2 [hep-ex] .

[5] Matthew Severson, Neutrino Mass and Proton Lifetime in a Realistic SUSY SO (10) Model, PHD Thesis ,https://inspirehep.net/record/1416836?ln=en, 2016.

[6] CDF Collaboration, Observation of Top Quark Production in $p\bar{p}$ Collisions with the Collider Detector at Fermilab, Phys. Rev. Lett. 74 (1995), 2626.

[7] D0 Collaboration, Search for High Mass Top Quark Production in pp Collisions at $\sqrt{s} = 1.8$ TeV, Phys. Rev. Lett. 74, 2422.

[8] Wikipidia, Top quark.https://en.wikipedia.org/wiki/Top_quark, March, 2017.

[9] D0 Collaboration, Determination of the pole and MSbar masses of the top quark from the $t\bar{t}$ cross section, arXiv:1104.2887v1 [hep-ex] .

[10] A. H. Hoang and I. W. Stewart, Top Mass Measurements from Jets and the Tevatron Top-Quark Mass, Nucl.Phys.Proc.Suppl.185:220-226, 2008 , arXiv:0808.0222v2 [hep-ph].

[11] ATLAS Top physics group, Summary plots, mtopSummary, March 2017.

[12] D. Buttazzo et al., Investigating the near-criticality of the Higgs boson, arXiv:1307.3536 [hep-ph].

[13] G. Degrassi et al., Higgs mass and vacuum stability in the Standard Model at NNLO, arXiv:1205.6497v2 [hep-ph].

[14] https://en.wikipedia.org/wiki/Hierarchy_problem#/media/File:Hqmc-vector.svg, March, 2017.

[15] http://gfitter.desy.de/Figures/Standard_Model/2014_07_16_Scan2D_MWvsmt_logo_large.gif, March, 2017.

[16] ATLAS Collaboration, Measurement of the Top Quark Mass with the Template Method in the $t\bar{t}$ $\rightarrow$ lepton+jets Channel using ATLAS data, Eur. Phys. J., C72:2046, (2012), arXiv:1203.5755 [hep-ex].

[17] ATLAS Collaboration. Measurement of the Top Quark Mass in Dileptonic Top Quark Pair Decays with $\sqrt{s} = 7$ TeV ATLAS data, ATLAS-CONF-2013-077.

[18] ATLAS collaboration, Measurement of the Top Quark Mass from $\sqrt{s} =$ 7 TeV ATLAS Data using a 3-dimensional Template Fit, Eur. Phys. J. C (2015) 75:330, arXiv:1503.05427 [hep-ex].

[19] ATLAS collaboration, Measurement of the top quark mass in topologies enhanced with single top-quarks produced in the t-channel in $\sqrt{s} = 8$ TeV ATLAS data, arXiv:1411.3879 [hep-ex].

[20] B. Roderik et al., LHC Run 2: Results and Challenges, CERN-ACC-2016-0103.

[21] ATLAS Experiment Multimedia, Gallery home-LHC, http://atlasexperiment.org/photos/lhc.html, March, 2017.

[22] ATLAS Collaboration, G. Aad et al., The ATLAS Simulation Infrastructure. Eur.Phys.J.C70:823-874,2010, arXiv:1005.4568v1.

[23] Matthias Schott and Monica Dunford, Review of single vector boson production in pp collisions at $\sqrt{s} = 7$ TeV, Eur. Phys. J. C (2014) 74:2916, arXiv:1405.1160v2 .

[24] ATLAS Experiment Multimedia, Gallery home - Inner Detector - Combined, http://atlasexperiment.org/photos/inner-detector-combined.html, March, 2017.

[25] ATLAS Experiment Multimedia, Gallery home - Calorimeters - Combined Barrel, http://atlasexperiment.org/photos/calorimeters-combined-barrel.html, March, 2017.

[26] ATLAS Experiment Multimedia, Gallery home - Muon Chambers, http://atlasexperiment.org/photos/muons-combined.html, March, 2017.

[27] A. Buckley et al., General-purpose event generators for LHC physics, arXiv:1101.2599 .

[28] M. Dobbs and J. B. Hansen, The HepMC C++ Monte Carlo event record for High Energy Physics, Comput. Phys. Communication. 134 , 41-46 (2001).

[29] C. Oleari, The POWHEG-BOX, Nucl.Phys.Proc.Suppl.205-206:36-41,2010, arXiv:1007.3893 [hep-ph].

[30] T. Sjostrand, PYTHIA 6.4 Physics and Manual, JHEP 0605:026,2006, arXiv:hep-ph/0603175.

[31] T. Gleisberg et. al, Event generation with SHERPA 1.1, JHEP 0902:007,2009, arXiv:0811.4622 [hep-ph].

[32] J. Bellm et al., Herwig 7.0 / Herwig++ 3.0 Release Note, arXiv:1512.01178 [hep-ph].

[33] J. Alwall et al., The automated computation of tree-level and next-to-leading order differential cross sections, and their matching to parton shower simulations, JHEP07(2014)079 , arXiv:1405.0301 [hep-ph].

[34] A. Knue, XsecSummarySingleTop, October, 2016.

[35] A. Knue, XsecSummaryTTbar , October, 2016.

[36] A. Knue, XsecSummaryDibosonSherpa , October, 2016.

[37] A. Knue MC15WjetsSherpaLightSamplesPMG , October, 2016.

[38] A. Knue, MC15WjetsSherpaCSamplesPMG, October, 2016.

[39] A. Knue, MC15WjetsSherpaBSamplesPMG, October, 2016.

[40] A. Knue, MC15ZjetsSherpaBSamplesPMG , October, 2016.

[41] A. Knue, MC15ZjetsSherpaLightSamplesPMG , October, 2016.

[42] A. Knue, MC15ZjetsSherpaCSamplesPMG, October, 2016.

[43] S. Agostinelli et al., Nucl. Instru.Meth. A506 (2003), pp. 250-303.

[44] ATLAS Experiment Multimedia, Gallery home - How ATLAS Works, http://atlasexperiment.org/photos/how-atlas-works.html, April, 2017.

[45] ATLAS Collaboration, Electron Reconstruction and Identification with the ATLAS Detector, Eur. Phys. J. C (2014) 74:2941, arXiv:1404.2240 [hep-ex].

[46] ATLAS Collaboration, Muon Reconstruction Performance, ATLAS-CONF-2010-064.

[47] W. Lampl et al., Calorimeter Clustering Algorithms : Description and Performance, ATL-COM-LARG-2008-003.

[48] M. Cacciari, G. Salam, and G. Soyez. The anti-k_t jet clustering algorithm, JHEP 0804:063,2008, arXiv:0802.1189 [hep-ph].

[49] The ATLAS collaboration, Commissioning of the ATLAS high-performance b-tagging algorithms in the 7 TeV collision data, ATLAS-CONF-2011-102.

[50] https://i1.wp.com/www.particlebites.com/wp-content/uploads/2016/08/B-tagging_diagram.png, April, 2017.

[51] ATLAS Collaboration, Performance of missing transverse momentum reconstruction in proton-proton collisions at 7 TeV with ATLAS, Eur.Phys.J.C 72 (2012) 1844, arXiv:1108.5602 [hep-ex]

[52] P. Sturm, T. Mueller, W. Wagner. Studies for the Measurement of Single-Top-Quark-Events with the CMS-Experiment, CMS-TS-2008-011.

[53] https://atlas.web.cern.ch/Atlas/GROUPS/DATAPREPARATION/PublicPlots/2015/DataSummary/figs/intlumivstime2015DQ.png, April, 2017.

[54] A. K. Becker and W. Wagner, Inclusive and differential cross-section measurements of t-channel single top-quark production at $\sqrt{s} = 7$ TeV with the ATLAS detector, CERN-THESIS-2014-325.

[55] ATLAS Collaboration, Measurement of the inclusive cross-sections of single top-quark and top-antiquark t-channel production in pp collisions at $\sqrt{s} = 13$ TeV with the ATLAS detector, arXiv:1609.03920v1 [hep-ex].

[56] https://www.otexts.org/fpp/9/3, April, 2017.

[57] G. COWAN, Statistical Data Analysis, United Kingdom: Oxford University Press, 1998.

[58] J. Pumplin, D. R. Stump, W. K. Tung, Multivariate Fitting and the Error Matrix in Global Analysis of Data, Phys.Rev.D65:014011,2001 arXiv:hep-ph/0008191

[59] ATLAS Collaboration, Jet energy measurement and its systematic uncertainty in proton-proton collisions at $\sqrt{s} = 7$ TeV with the ATLAS detector, Eur. Phys. J. C (2015) 75:17, arXiv:1406.0076 [hep-ex].

[60] ATLAS Collaboration, Jet energy measurement with the ATLAS detector in proton-proton collisions at $\sqrt{s} = 7$ TeV, Eur. Phys. J. C, 73 3 (2013) 2304 arXiv:1112.6426 [hep-ex].

[61] A. Knue, TopSystematicUncertainties for 8 TeV 2012 analyses (rel17.2), https://twiki.cern.ch/twiki/bin/view/AtlasProtected/TopSystematicUncertainties#MET, April, 2016.

[62] I. Nugent, TopETmissLiaison-EPS, https://twiki.cern.ch/twiki/bin/viewauth/AtlasProtected/TopETmissLiaison_EPS#LAr_Hole, 2011.

[63] F. Fabbri, TopSystematicUncertainties for early 13 TeV Analyses, https://twiki.cern.ch/twiki/bin/view/AtlasProtected/TopSystematics13TeV, February, 2017.

[64] ATLAS Collaboration, Calibration of b-tagging using dileptonic top pair events in a combinatorial likelihood approach with the ATLAS experiment, ATLAS-CONF-2014-004.

[65] ATLAS Collaboration, LuminosityPublicResultsRun2.